Lithos 320–321 (2018) 265–279

Contents lists available at ScienceDirect

Lithos

journal homepage: www.elsevier.com/locate/lithos

The genetic relationship between JTA–like magmas and typical adakites: An example from the Late Cretaceous Nuri complex, southern Tibet

Chang-da Wu [a], Yuan-chuan Zheng [a,*], Bo Xu [b], Zeng-qian Hou [c]

[a] School of Earth Sciences and Resources, China University of Geosciences, Beijing 100083, PR China
[b] School of Gemmology, China University of Geosciences, Beijing 100083, PR China
[c] Institute of Geology, Chinese Academy of Geological Sciences, Beijing 100037, PR China

ARTICLE INFO

Article history:
Received 1 June 2018
Accepted 26 September 2018
Available online 28 September 2018

Keywords:
Adakites
JTA–like magmas
Geochemistry
Fractional crystallization
Southern Tibet

ABSTRACT

Phanerozoic adakites typically represent modern analogues of Middle–Late Archean (3.5–2.5 Ga) tonalite–trondhjemite–granodiorite rocks (TTGs) due to their similarities in geochemical compositions. However, no Phanerozoic analogues have been reported for the Early Archean TTGs (>3.5 Ga), which are characterized by low Sr, Y and HREEs contents with low MgO and compatible elements contents, until recent years. The newfound Phanerozoic analogues have been defined as a new adakite subgroup named as "Jamaican–type adakites" (JTAs), and been regarded as the results of partial melting of subducted oceanic plateau crust. JTA–like magmas also occur in the Nuri complex, southern Tibet. We report whole–rock geochemical, Sr—Nd isotopic data, zircon U—Pb ages and in-situ Hf isotopic data for adakitic quartz diorites, quartz monzonites and JTA–like quartz porphyries in the Nuri complex. Zircon U—Pb dating indicates that these rocks were emplaced in the Late Cretaceous at 93.5–92.1 Ma. Combined with the continuous variation trends of major and trace elements, the similarities in terms of whole–rock Sr—Nd and zircon Hf isotopic compositions indicate that the three types of rocks are genetically related, while the quartz diorites should represent the relatively primitive melts. High MgO (5.00–5.41 wt%), Cr (138–159 ppm), Ni (65.9–96.8 ppm) contents and Mg# values (66–69), high $\varepsilon_{Hf}(t)$ values (10.5–11.9), $\varepsilon_{Nd}(t)$ values (3.7), and low $(^{87}Sr/^{86}Sr)_i$ values (0.7046–0.7050) indicate that the quartz diorites were derived from partial melting of subducted Neo–Tethyan oceanic slab, and subsequently underwent metasomatic reaction with the mantle wedge during their ascent. Quartz monzonites and JTA–like quartz porphyries were originated from quartz diorites by two stages of fractional crystallization. Low MgO and compatible elements contents of the quartz porphyries were caused by fractionation of hornblende, biotite, with minor magnetite and allanite, while low Sr contents and Sr/Y ratios were mainly controlled by plagioclase fractionation. This means that the JTA–like geochemical features of the quartz porphyries were generated by fractional crystallization from the adakites derived from partial melting of subducted slab, rather than directly derived from partial melting of subducted oceanic plateau. Therefore, various petrogenetic possibilities of the JTA–like magmas should be considered when using them as modern analogues.

1. Introduction

"Adakite" was first introduced by Defant and Drummond (1990) to define a rock type generated specifically by partial melting of young and hot subducted oceanic crust, based on the work of Kay (1978) on magnesian andesites from Adak Island. As originally defined, the adakites have $SiO_2 \geq 56$ wt%, $Al_2O_3 \geq 15$ wt% (rarely lower), usually MgO < 3 wt% (rarely above 6 wt%), low heavy rare earth elements (HREEs) and Y contents (e.g., Yb ≤ 1.9 ppm, Y ≤ 18 ppm), typically Sr ≥ 400 ppm and low high field strength elements (HFSEs) (Defant and Drummond, 1990). Apart from oceanic subduction settings, igneous rocks with adakitic geochemical features have also been identified in several other tectonic settings, like collisional orogenic zones and intra–continental settings (e.g., Chung et al., 2003; Hou et al., 2004; Wang et al., 2007; Xu et al., 2002). Consequently, various other genetic models have been proposed, such as (1) partial melting of thickened mafic lower crust (Chung et al., 2003; Hou et al., 2004), (2) partial melting of delaminated lower continental crust (Wang et al., 2007; Xu et al., 2002), (3) crustal assimilation and fractional crystallization (AFC) process of parental basaltic magmas (Castillo et al., 1999; Macpherson et al., 2006), and (4) magma mixing between felsic and basaltic magmas (Guo et al., 2007; Streck et al., 2007). These rocks are commonly named as "adakite–like rocks", since they have adakitic compositions but their source regions are different from the typical adakites.

In order to constrain the origin of the adakitic rocks, Martin et al. (2005) divided them into (1) low–SiO_2 adakitic rocks (LSA) that

* Corresponding author: School of Earth Sciences and Resources, China University of Geosciences, 29# Xueyuan Road, Haidian District, Beijing 100083, PRChina.
E-mail address: zhengyuanchuan@gmail.com (Y. Zheng).

https://doi.org/10.1016/j.lithos.2018.09.031
0024-4937/

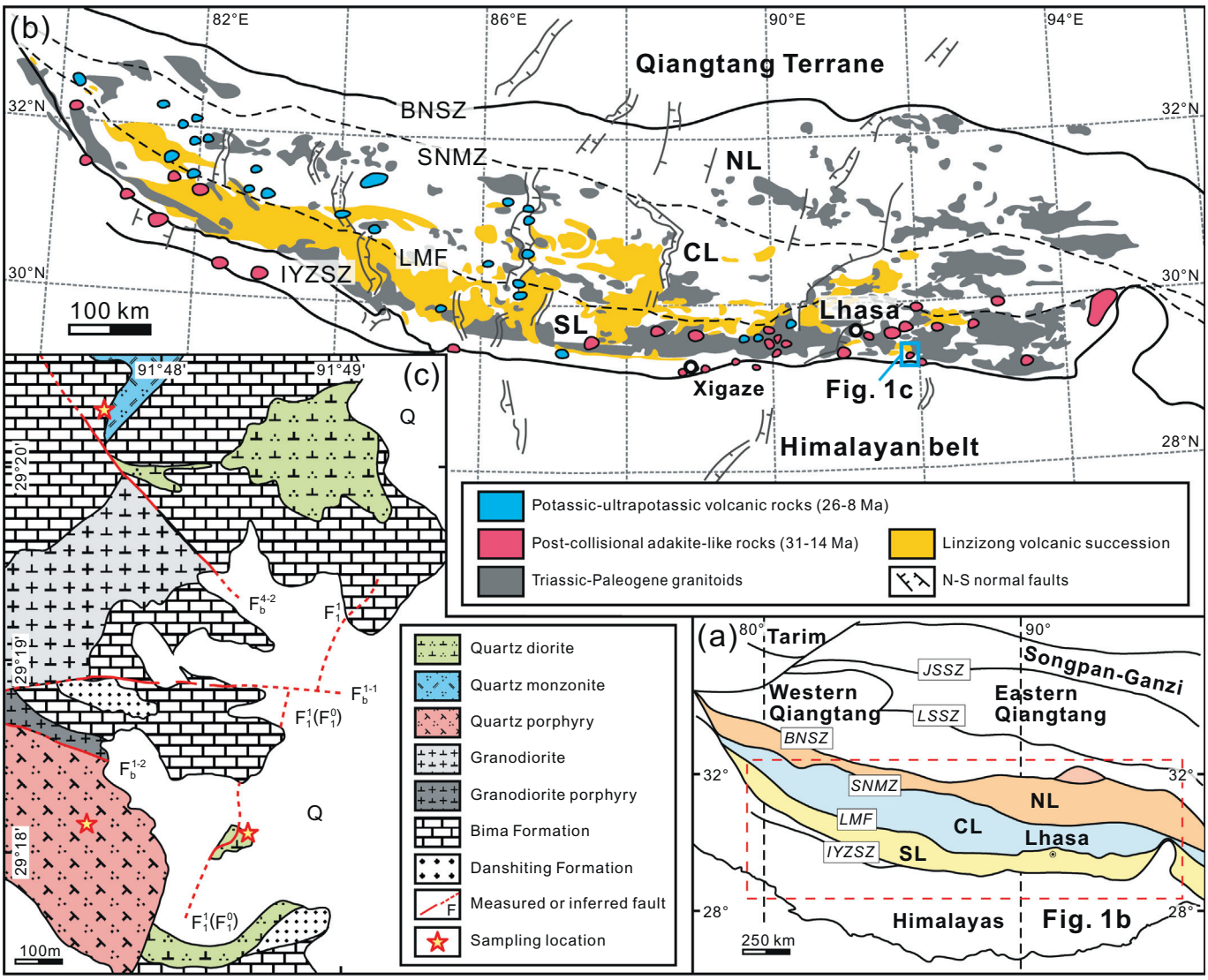

Fig. 1. (a) Sketch map showing the Lhasa terrane in the context of the Tibetan Plateau (modified from Zhu et al., 2011); (b) Simplified geologic map of the Lhasa terrane showing the major tectonic subdivisions and the distribution of Phanerozoic igneous rocks (modified from Zheng et al., 2012a); (c) Geological map showing outcrops of Nuri complex on the southern margin of the Lhasa terrane (modified from Chen et al., 2015). Abbreviations: JSSZ = Jinsha suture zones, LSSZ = Longmu Tso–Shuanghu suture zone, BNSZ = Bangong–Nujiang suture zones, SNMZ = Shiquan River–Nam Tso Mélange Zone, LMF = Luobadui–Milashan Fault, IYZSZ = Indus–Yarlung Zangbo suture zones, NL = northern Lhasa subterrane, CL = central Lhasa subterrane, and SL = southern Lhasa subterrane.

represent the adakitic melts generated by partial melting of mantle wedge metasomatised by felsic slab melts, and (2) high–SiO_2 adakitic rocks (HSA) that represent the typical adakites and are thought to be derived from partial melting of subducted oceanic slab followed by interaction with overlying mantle wedge. Recent years, a new subgroup of adakites, named as "Jamaican–type adakites" (JTAs), has been defined by Hastie et al. (2010a, 2010b, 2015). The JTAs have adakitic compositions and are similar to HSA with high SiO_2 contents and $(La/Yb)_n$ ratios as well as low HREEs and Y contents. However, there also exist some compositional differences between JTAs and HSA, which make JTAs unique. The key differences are that the JTAs are characterized by low Sr contents and Sr/Y ratios, as well as low MgO and compatible elements contents. These features have been interpreted as the results of partial melting of subducted oceanic plateau crust leaving a residue of hornblende, garnet and plagioclase. Meanwhile, the JTAs have been taken as a modern analogue of Early Archean tonalite–trondhjemite–granodiorite rocks (TTGs) (Hastie et al., 2010a, 2010b, 2015), due to their comparable geochemical compositions (Martin et al., 2005; Martin and Moyen, 2002; Smithies, 2000). However, Shuto et al. (2013) argued that the JTA–like rhyodacites identified in the northeastern Japan arc could be generated by fractional crystallization of normal arc magmas, implying that petrogenesis of the JTAs or JTA–like magmas should be further investigated.

Both typical adakites and JTA–like magmas have been found in the Nuri complex in southern Tibet, indicating that it should be one of the ideal places to address the petrogenesis of the JTAs or JTA–like magmas. In this paper, we present whole–rock geochemical, Sr—Nd isotopic data, zircon U—Pb ages and in-situ Hf isotopic data, for adakitic quartz diorites, quartz monzonites, and JTA–like quartz porphyries in the Nuri complex. These data provide constraints on the petrogenesis of the Late Cretaceous Nuri complex and provide new insights into the genetic relationship between JTA–like magmas and typical adakites.

2. Geological background and rock characteristics

The Tibetan Plateau comprises a series of east–west trending terranes: from north to south, they are the Songpan–Ganzi, Qiangtang, Lhasa, and Himalayan terranes. These four terranes are separated by the Jinsha suture zones (JSSZ), Bangong–Nujiang suture zones (BNSZ), and Indus–Yarlung Zangbo suture zones (IYZSZ), respectively (Yin and

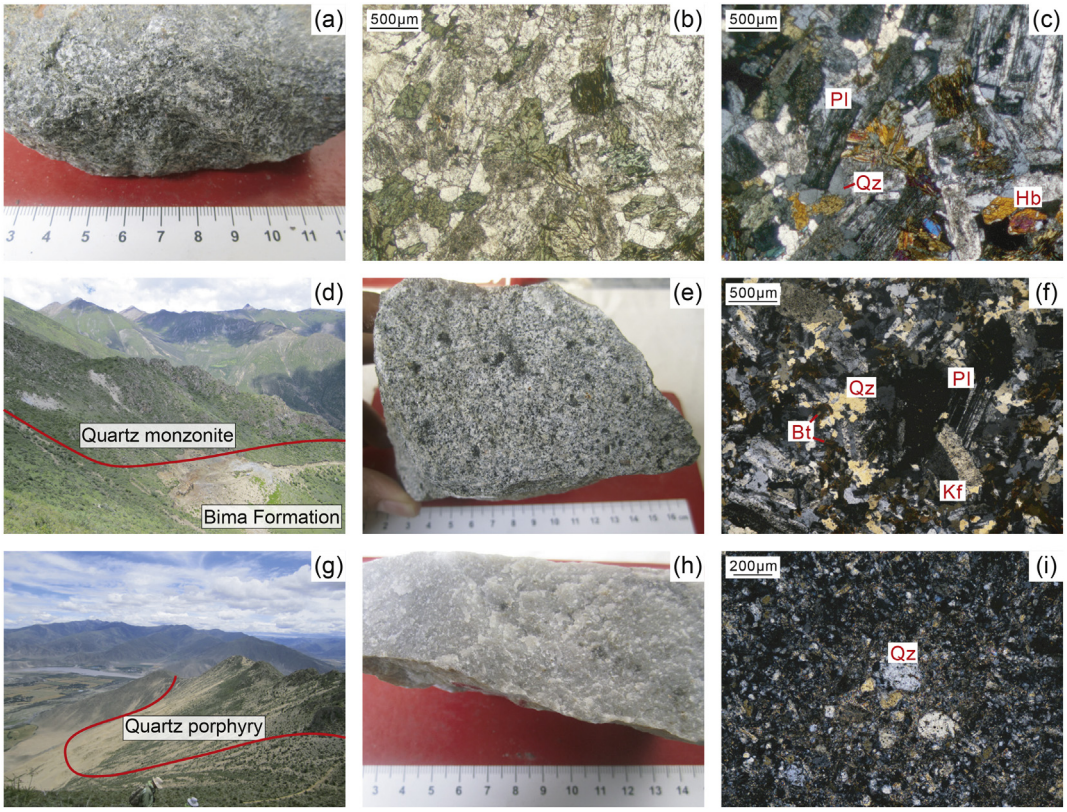

Fig. 2. Field photographs and microphotographs of the Nuri complex. (a) Field photograph of quartz diorite; (b–c) Microphotographs of quartz diorite; (d–e) Field photographs of quartz monzonite; (f) Microphotograph of quartz monzonite; (g–h) Field photographs of quartz porphyry; (i) Microphotograph of quartz porphyry. Abbreviations: Bt = biotite, Kf = K–feldspar, Hb = hornblende, Pl = plagioclase, Qz = quartz.

Harrison, 2000) (Fig. 1a–b). The Lhasa terrane is bounded to the south by the IYZSZ which resulted from the northward drift of the Indian plate and its subsequent collision with the Asian plate at ca. 55–50 Ma (Meng et al., 2012; Zhu et al., 2015). The northern boundary of the Lhasa terrane is BNSZ which was caused by the closure of the Bangong–Nujiang Ocean due to continental collision between the Lhasa and Qiangtang terranes during the Late Jurassic to Early Cretaceous (Yin and Harrison, 2000; Zhu et al., 2009a). According to the differences in sedimentary cover and basement, the Lhasa terrane can be further divided into northern, central, and southern subterrane, separated by the Shiquan River–Nam Tso Mélange Zone (SNMZ) and Luobadui–Milashan Fault (LMF) (Zhu et al., 2009a). This is supported by recent studies of zircon Hf isotopic mapping (Hou et al., 2015; Zhu et al., 2011). The central Lhasa subterrane was once a microcontinent with a Proterozoic and Archean basement, and are mainly covered by the widespread Permo–Carboniferous metasedimentary rocks and Late Jurassic–Early Cretaceous volcano–sedimentary rocks (Pan et al., 2004; Zhu et al., 2009a, 2011). During the northward drift of the central Lhasa subterrane and its subsequent continental collision, juvenile crust accreted at its both edges and formed the southern and northern Lhasa subterranes (Hou et al., 2015; Zhu et al., 2011). Precambrian basement rocks are probably absent from the northern Lhasa subterrane and the sedimentary cover is composed of the Jurassic–Cretaceous with minor Triassic sedimentary rocks and Early Cretaceous volcanic rocks (Pan et al., 2004; Zhu et al., 2011). In the southern Lhasa subterrane, Precambrian basement rocks are locally present in its eastern segment (Dong et al., 2010). The sedimentary cover is also limited and largely restricted to the eastern part of the southern Lhasa subterrane, which mainly consists of the Late Triassic–Cretaceous clastic sedimentary rocks and abundant volcanic rocks (Pan et al., 2004; Zhu et al., 2008).

The Gangdese magmatic belt, located at the southern margin of the Lhasa terrane, is subparallel to the IYZSZ and trends east–west for a distance exceeding 2000 km. Attributed to the subduction of Neo–Tethyan oceanic slab and the subsequent collision between the Indian and Asian plate, voluminous intrusive rocks and widespread volcanic rocks occur in the Gangdese belt. The intrusive rocks consist of pre– to syn–collisional Gangdese batholith and post–collisional intrusions. The Gangdese batholith records a long–period of magmatism from the Late Triassic to Eocene (ca. 210–40 Ma), with activity peaking at 109–76 Ma and 65–41 Ma (e.g., Ji et al., 2009; Wen et al., 2008b; Zheng et al., 2014; Zhu et al., 2011). The post–collisional intrusive rocks commonly have geochemical affinities with adakites, and they were emplaced in Oligocene–Miocene and intruded into the Gangdese batholith and volcanic–sedimentary formations as small–volume stocks or dykes (e.g., Chung et al., 2003; Hou et al., 2004, 2013; Zheng et al., 2012a, 2012b). In the Gangdese belt, the extensive volcanic rocks are mainly composed of the Early Jurassic Yeba Group volcanic rocks, the Early Jurassic–Early Cretaceous Sangri Group volcanic rocks, the Late Cretaceous–Eocene Linzizong volcanic rocks and the Oligocene–Miocenepotassic–ultrapotassic volcanic rocks (e.g., Kang et al., 2014; Zhao et al., 2009; Zhu et al., 2008, 2009b, 2015).

The Nuri complex, which is located at the southern margin of Gangdese belt and approximately 9 km northeast of Zedong town, southern Tibet, is intruded into the Early Cretaceous Bima Formation of the Sangri Group. The complex mainly consists of quartz diorite, quartz monzonite, quartz porphyry, granodiorite and granodiorite porphyry (Fig. 1c), while only the former three types of rocks with similar ages of emplacement have been studied here. The quartz diorite has a medium–grained igneous texture and is mainly composed of plagioclase (60–70%), hornblende (10–25%), quartz (5–10%), and biotite (ca. 5%), with minor K–feldspar and accessory minerals including zircon, apatite and Fe—Ti oxides (Fig. 2a–c). The quartz monzonite exhibits a fine–grained igneous texture and contains quartz (10–20%), plagioclase (30–45%), K–feldspar (25–35%), hornblende (10–15%), biotite (ca. 5%) and minor accessory minerals (zircon, apatite and Fe—Ti oxides)

(Fig. 2d–f). The quartz porphyry shows a porphyritic texture and its phenocrysts are dominated by rounded corroded quartz (Fig. 2g–i).

3. Methods

3.1. Zircon U—Pb dating

Zircon grains used for dating were separated by standard density and magnetic techniques before finally being hand–picked under a binocular microscope, and then mounted in an epoxy resin and polished down to approximately half section to expose the grain centers. Prior to analytical work, all zircon grains were examined under a microscope with transmitted and reflected light as well as cathodoluminescence (CL) images using a scanning electron microscope (CL–SEM) to reveal their internal structures. Zircon U—Pb dating and trace elements analyses were conducted using laser ablation inductively coupled plasma mass spectrometry (LA–ICP–MS) at the State Key Laboratory of Geological Processes and Mineral Resources, China University of Geosciences, Wuhan. Laser sampling was performed using an excimer laser ablation system (GeoLas 2005), and ion–signal intensities were acquired by ICP–MS instrument (Agilent 7500a). The diameter of spot was 32 μm. The detailed operating conditions for the laser sampling system and the ICP–MS instrument were described by Liu et al. (2010). Off–line selection, integration of background and analyte signals, time–drift correction, and quantitative calibration for trace element analyses and U—Pb dating were performed by ICPMSDataCal. The common lead was corrected using LA–ICP–MS Common Lead Correction (ver. 3.15), followed the method of Andersen (2002). Concordia ages and diagrams were obtained using Isoplot/Ex (3.0) (Ludwig, 2003).

3.2. Zircon Lu—Hf isotope measurements

In-situ zircon Lu—Hf isotope measurements were performed using a Neptune MC–ICP–MS equipped with a 193–nm laser at the Institute of Geology and Geophysics, Chinese Academy of Sciences, Beijing. The Hf isotopic composition analyses were carried out on the same spots that were previously analyzed for U—Pb dating, with a beam size of 63 μm and an ablation time of 26 s. Zircon GJ–1 and Mud Tank were used as reference standards. The detailed instrumental conditions and data acquisition can be found in Wu et al. (2006). The decay constant for ^{176}Lu is 1.867×10^{-11} yr^{-1}(Söderlund et al., 2004). The $\varepsilon_{Hf}(t)$ values were calculated relative to the chondritic reservoir (CHUR) which has a $^{176}Hf/^{177}Hf$ ratio of 0.282772 and $^{176}Lu/^{177}Hf$ of 0.0332 (Blichert Toft and Albarède, 1997). The depleted mantle model ages (T_{DM}) were calculated relative to the depleted mantle at a present–day $^{176}Hf/^{177}Hf$ ratio of 0.283250 and $^{176}Lu/^{177}Hf$ of 0.0384 (Griffin et al., 2000). The Hf isotopic "crustal" model age (T_{DM}^{C}) were also calculated by assuming that the parental magma has been derived from an average continental crust (MC), with $^{176}Lu/^{177}Hf$ ratio of 0.015, that originated from the depleted mantle (Griffin et al., 2002).

3.3. Whole–rock major and trace elements

Samples for geochemical analyses were ground to pass through a 200 mesh and further ground and homogenized in an agate mortar under alcohol. Major element oxides, trace elements and rare earth elements (REEs) of those samples were analyzed by X–ray fluorescence (XRF) and by inductively coupled plasma mass spectrometry (ICP–MS), respectively, at the National Research Centre for Geoanalysis, Chinese Academy of Geological Science, Beijing. The analytical uncertainty of XRF analyses for major elements was within 5%, and the uncertainty of the elements examined here was also <5% for the ICP–MS analyses.

3.4. Whole–rock Sr—Nd isotopes

Whole–rock Sr—Nd isotopic analyses were performed using a Triton mass spectrometer (TIMS) at the Isotope Geology Lab, Chinese Academy of Geological Sciences, Beijing. For the NBS–987 standard, the $^{87}Sr/^{86}Sr$ ratio was 0.71025 ± 2 (2σ). The measurement accuracy of the Rb/Sr ratio was better than 0.1% and the mass fractionation of Sr isotopes was corrected with $^{88}Sr/^{86}Sr$ ratio of 8.37521. The Johnson–Matthey $^{143}Nd/^{144}Nd$ ratio was 0.511125 ± 8 (2σ), while the measurement accuracy of the Sm/Nd ratio was also better than 0.1% and the mass fractionation of Nd isotopes was corrected by using $^{146}Nd/^{144}Nd$ value of 0.7219. The $^{87}Rb/^{86}Sr$ and $^{147}Sm/^{144}Nd$ ratios were calculated using the Rb, Sr, Sm and Nd contents obtained by ICP–MS.

3.5. Trace element modeling

The fractional crystallization process was quantitatively estimated in this study by using the Raleigh equation:

$$C^i = C_o^i \times (1-F)^{D^i-1}$$

where C^i and C_o^i represent the contents of element i in the resulting melts and in the initial materials, respectively, and F is the degree of fractional crystallization. D^i is the bulk partition coefficient of element i, which can be calculated by using equation:

$$D^i = \sum_{j=1}^{n} k_j^i \times W_j$$

where k_j^i is the mineral/melt partition coefficient of mineral j and element i, W_j is the mass proportion of mineral j in the total crystallized minerals, and n is the number of the crystallized mineral phases. Mineral/melt partition coefficients used here are listed in Table S4.

4. Results

4.1. Zircon U—Pb geochronology

Samples NR11–30–2–1, NR–32 and NR–9 were collected from the Nuri quartz diorite, quartz monzonite and quartz porphyry, respectively. Most zircon grains from these samples are characterized by euhedral to subhedral crystal shapes exhibiting long to short prismatic forms, with average crystal lengths of ca. 70–300 μm and length–to–width ratios ranging from 1:1 to 5:1. Zircon grains commonly are transparent and colorless, and show euhedral oscillatory or planar zoning in CL images (Fig. S1). All the results of zircon U—Pb dating are listed in Table S1, and presented on Concordia diagrams with 1σ errors in Fig. 3.

Zircons from quartz diorite (NR11–30–2–1) yield $^{206}Pb/^{238}U$ ages ranging from 88.0 to 98.5 Ma for twenty–two spot analyses, which have a weighted mean $^{206}Pb/^{238}U$ age of 92.1 ± 0.9 Ma (MSWD = 0.86; Fig. 3a–b). Eighteen analyzed spots from quartz monzonite (NR–32) have similar $^{206}Pb/^{238}U$ ages ranging from 92.2 to 94.0 Ma, with a weighted mean $^{206}Pb/^{238}U$ age of 93.0 ± 1.4 Ma (MSWD = 0.026; Fig. 3c–d). Sixteen analyses from quartz porphyry (NR–9) yield zircon $^{206}Pb/^{238}U$ ages ranging from 91.0 to 98.8 Ma, with a weighted mean $^{206}Pb/^{238}U$ age of 93.5 ± 1.5 Ma (MSWD = 0.50; Fig. 3e–f).

4.2. Zircon Lu—Hf isotopes

The zircon Lu—Hf isotopic data and detailed calculation formulas are listed in Table S2. Ten Lu—Hf analyses obtained on zircon grains from the Nuri quartz diorite (NR11–30–2–1) yield $^{176}Hf/^{177}Hf$ ratios of 0.283017 to 0.283054, corresponding to $\varepsilon_{Hf}(t)$ values of 10.5 to 11.9.

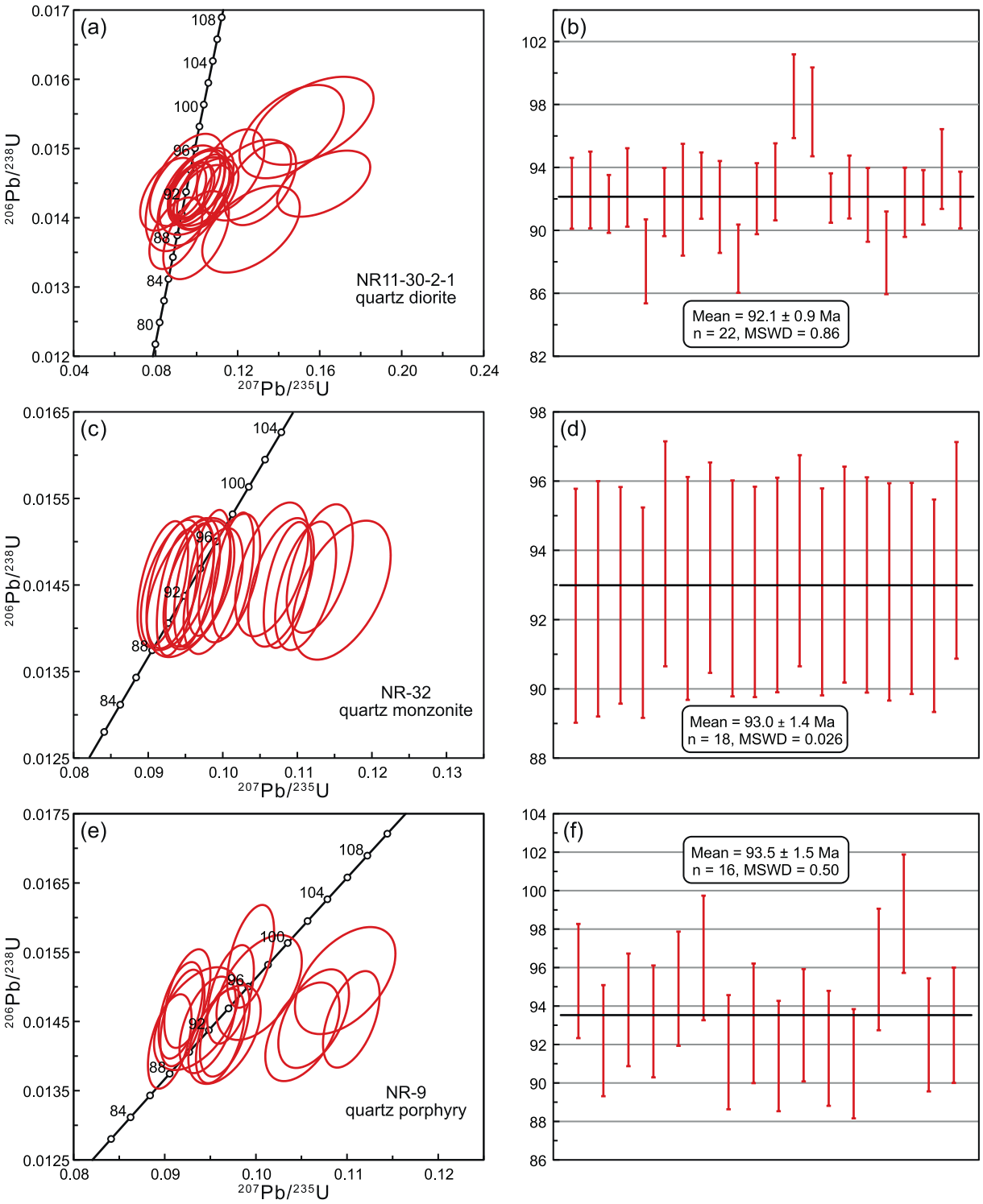

Fig. 3. U—Pb ages of zircons from (a–b) quartz diorite (NR11–30–2–1), (c–d) quartz monzonite (NR–32), and (e–f) quartz porphyry (NR–9) from the Nuri complex, southern Tibet.

Model ages calculated relative to the depleted mantle (T_{DM}) range from 279 to 329 Ma, and the crustal model ages (T_{DM}^{C}) vary from 393 to 479 Ma. Fourteen analyzed spots from the Nuri quartz monzonite (NR–32) have $^{176}Hf/^{177}Hf$ ratios of 0.283030 to 0.283190, with positive $\varepsilon_{Hf}(t)$ values ranging from 11.1 to 16.8. They have T_{DM} ages of 85 to 322 Ma and T_{DM}^{C} ages of 80 to 447 Ma. Fifteen spots on zircons from the Nuri quartz porphyry (NR–9) show $^{176}Hf/^{177}Hf$ ratios ranging from 0.283029 to 0.283158, corresponding to $\varepsilon_{Hf}(t)$ values of 10.9 to 15.5. Their T_{DM} ages and T_{DM}^{C} ages range from 137 to 337 Ma and 161 to 457 Ma, respectively.

4.3. Whole–rock major and trace elements

The whole–rock major and trace element data for the Nuri quartz diorites, quartz monzonites and quartz porphyries are presented in Table S3. The quartz diorites are medium– to high–Kcalc–alkaline and

metaluminous, with SiO_2 contents of 56.56 to 58.46 wt%, K_2O contents of 0.81 to 2.28 wt% and A/CNK values of 0.70 to 0.81 (Fig. 4a–b). They are characterized by high MgO contents of 5.00 to 5.41 wt% and Mg# values of 66 to 69, with high compatible elements contents (e.g., Cr, 138–159 ppm; Ni, 65.9–96.8 ppm). In the chondrite–normalizedREE patterns, the quartz diorites exhibit negligibly negative Eu anomalies (Eu/Eu* = 0.87–0.95) and fractionated REE patterns, with high $(La/Yb)_n$ ratios of 15.4 to 17.2, low HREEs contents (e.g., Yb, 1.10–1.15 ppm) and Y contents of 13.2 to 13.9 ppm (Fig. 5a). These characteristics, together with high Sr contents of 667 to 836 ppm and Sr/Y ratios of 48.1 to 63.5, indicate that the samples have geochemical affinities with adakites (Fig. 4c–d). In addition, quartz diorites show enrichment in large ion lithophile elements (LILEs) relative to HFSEs, negative Nb–Ta–Ti and positive Pb anomalies in the primitive mantle–normalized incompatible element patterns (Fig. 5b).

The quartz monzonites belong to medium–Kcalc–alkaline to shoshonitic series, with SiO_2 contents of 59.03 to 65.67 wt% and variable K_2O contents ranging from 2.07 to 4.50 wt%. Except for sample NR–30 with peraluminous characteristics (A/CNK = 1.38), the samples mainly plot in metaluminous field, with A/CNK values of 0.68 to 1.06 (Fig. 4a–b). They have Mg# values of 51 to 67, MgO contents of 2.22 to 4.09 wt %, Cr contents of 38.9 to 116 ppm and Ni contents of 22.0 to 56.7 ppm. Quartz monzonites also have low contents of HREEs and Y (e.g., Yb, 0.75–1.00 ppm; Y, 9.47–11.9 ppm) and high Sr contents ranging from 244 to 1044, with high $(La/Yb)_n$ ratios of 14.4 to 22.2 and Sr/Y ratios of 25.0 to 95.9. In the Sr/Y versus Y and $(La/Yb)_n$ versus Yb_n diagrams, they all plot within the adakites fields (Fig. 4c–d). They have lower contents of REEs than the quartz diorites, and exhibit negligibly negative and positive Eu anomalies (Eu/Eu* = 0.80–1.07) (Fig. 5a). In the primitive mantle–normalized incompatible element patterns, quartz monzonites are characterized by enrichment in LILEs and depletion in HFSEs, as well as negative Nb–Ta–Ti and positive Pb anomalies, which is similar to those of the quartz diorites (Fig. 5b).

The quartz porphyry samples are high–Kcalc–alkaline and peraluminous, with high SiO_2 contents of 74.43 to 76.31 wt%, K_2O contents of 3.94 to 4.73 wt% and A/CNK values of 1.20 to 2.65 (Fig. 4a–b). They have low MgO contents of 0.30 to 0.47 wt% and Mg# values of 33 to 57, as well as low compatible elements contents (e.g., Cr, 3.34–6.60 ppm; Ni, 2.05–2.97 ppm). In the chondrite–normalizedREE patterns, quartz porphyry samples show slightly negative and negligibly positive Eu anomalies (Eu/Eu* = 0.76–1.03) and fractionated REE patterns, with high $(La/Yb)_n$ ratios of 15.6 to 19.7, low HREEs contents (e.g., Yb, 0.79–0.90 ppm) and Y contents of 7.37 to 8.04 ppm. They have the lowest REEs contents of all rock samples studied in this

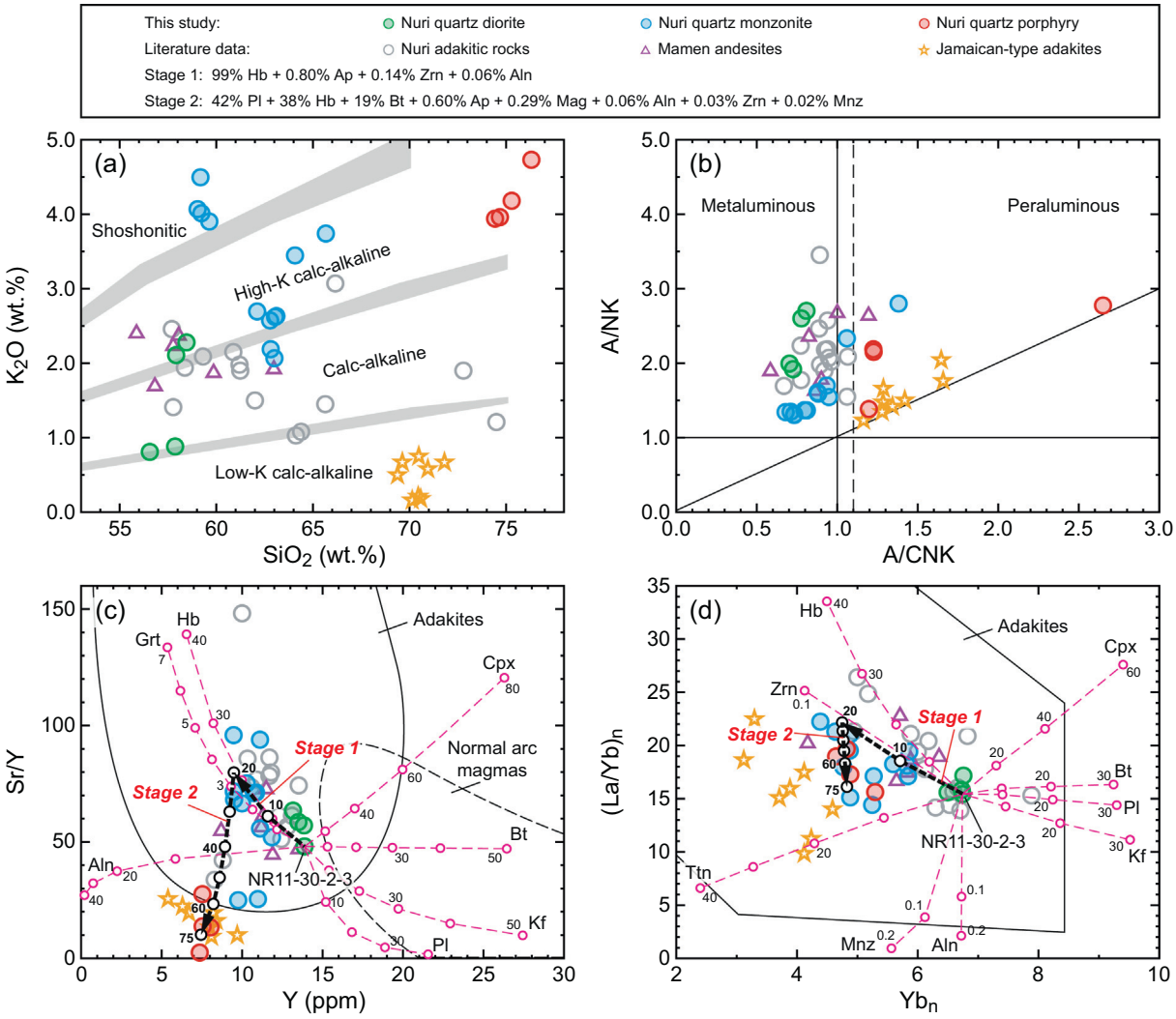

Fig. 4. (a) K_2O versus SiO_2(Peccerillo and Taylor, 1976); (b) A/NK (Al_2O_3 /(Na_2O + K_2O)) versus A/CNK (Al_2O_3/(CaO + Na_2O + K_2O)); (c) Sr/Y versus Y and (d) $(La/Yb)_n$ versus Yb_n diagrams for the Nuri complex, southern Tibet. The fields of adakites and normal arc magmas are from Defant and Drummond (1990) and Martin (1999). Chondrite normalizing values are from Sun and McDonough (1989). Mineral/melt partition coefficients are listed in Table S4. Data for Nuri adakitic rocks are from Zheng et al. (2014) and Chen et al. (2015). Data for Mamen andesites are from Zhu et al. (2009b). Data for Jamaican–type adakites are from Hastie et al. (2010a). Abbreviations: Aln = allanite, Bt = biotite, Cpx = clinopyroxene, Grt = garnet, Hb = hornblende, Kf = K–feldspar, Mnz = monazite, Pl = plagioclase, Ttn = titanite, Zrn = zircon.

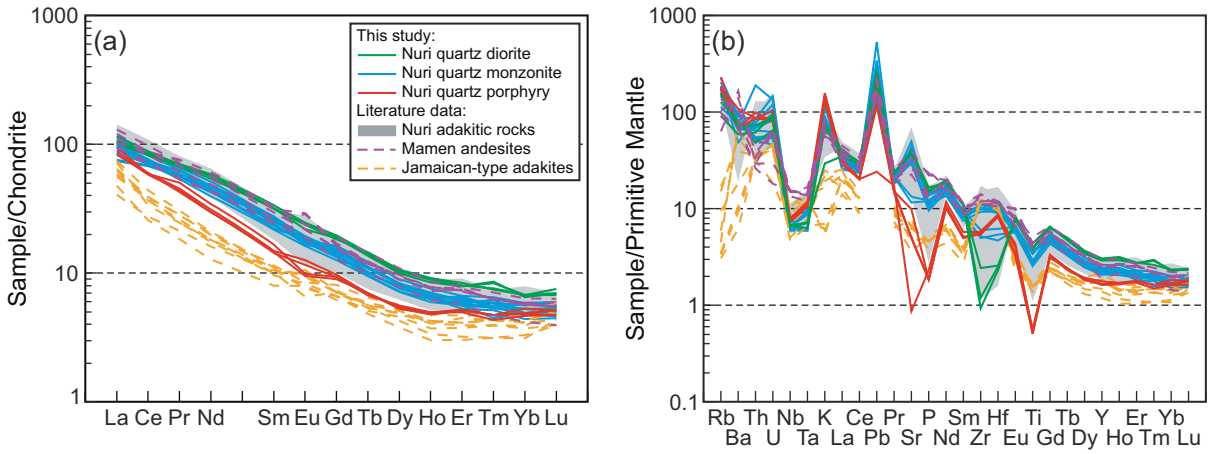

Fig. 5. (a) Chondrite–normalized REE patterns, and (b) Primitive mantle–normalized trace element patterns for the Nuri complex, southern Tibet. Chondrite and primitive mantle normalizing values are from Sun and McDonough (1989). Data are from the same source as Fig. 4.

study, and are depleted in middle REEs (MREEs) relative to light REEs (LREEs) and HREEs (Fig. 5a). Similar to primitive mantle–normalized incompatible element patterns for quartz diorites and quartz monzonites, quartz porphyries are also enriched in LILEs and depleted in HFSEs. They also have the lowest contents of Sr, P and Ti (Fig. 5b). Though the low contents of Sr (18.3–208 ppm) result in that quartz porphyry samples mainly plot below the field of adakites in the Sr/Y versus Y diagram, they all plot within the adakites field in the $(La/Yb)_n$ versus Yb_n diagram (Fig. 4c–d).

4.4. Whole–rock Sr—Nd isotopes

The whole–rock Sr—Nd isotopic data are listed in Table S3. Initial isotopic ratios of the Nuri quartz diorites, quartz monzonites and quartz porphyries were calculated based on their zircon U—Pb ages. All three types of rocks show similar whole–rock Sr—Nd isotopic data. The quartz diorites have $(^{87}Sr/^{86}Sr)_i$ values of 0.7046 to 0.7050 and $\varepsilon_{Nd}(t)$ values are both at 3.7, while the quartz monzonites have $(^{87}Sr/^{86}Sr)_i$ values of 0.7040 to 0.7044 and $\varepsilon_{Nd}(t)$ values of 3.1 to 4.1. The quartz porphyry samples show $(^{87}Sr/^{86}Sr)_i$ values of 0.7039 to 0.7040 and $\varepsilon_{Nd}(t)$ values of 3.8 to 3.9.

5. Discussion

5.1. Ages of the Nuri complex

The relatively high Th/U ratios ranging from 0.31 to 2.20 and the well–developed oscillatory or planar growth zoning in the zircons from the Nuri complex indicate that they are all of magmatic origin (Griffin et al., 2002; Hoskin and Schaltegger, 2003). Without complicated core–rim textures, zircons from the Nuri complex have close U—Pb ages (Fig. 3), indicating that the weighted mean $^{206}Pb/^{238}U$ ages should represent the timing of emplacement and crystallization of the complex. Therefore, the quartz diorite (NR11–30–2–1), quartz monzonite (NR–32) and quartz porphyry (NR–9) should emplace at 92.1 ± 0.9 Ma, 93.0 ± 1.4 Ma and 93.5 ± 1.5 Ma, respectively, which is consistent with the results of previous studies (96.0–91.1 Ma, Zheng et al., 2014; Chen et al., 2015).

5.2. Origin of the Nuri complex

5.2.1. Petrogenesis of the Nuri complex

Combined with similarity in emplacement age, continuous variation trends between SiO_2 and other major elements (Fig. 6) imply that rocks in the Nuri complex should be genetically related to each other. These continuous variation trends could be produced either by magma mixing between a relatively felsic magma and a relatively mafic magma, or by fractional crystallization of a relatively mafic parental magma.

The possibility that such variation trends are the results of magma mixing can be ruled out by following three reasons. Firstly, the injection of mafic magmas would leave a large number of mafic enclaves in the intermediate–felsic intrusive rocks (Guan et al., 2012; Zheng et al., 2012b, 2016). However, mafic enclaves are absent in the Nuri complex. Secondly, magma mixing would result in linear geochemical trends in Harker diagrams, which are inconsistent with the variation trends shown in the Al_2O_3 and Na_2O versus SiO_2 diagrams for the Nuri complex (Fig. 6e–f). Thirdly, according to the magma mixing model, the mafic end–member and felsic end–member typically have large differences but show binary mixing trends in isotopic compositions (Yang et al., 2004; Zheng et al., 2016), which is inconsistent with the similar Sr–Nd–Hf isotopic data observed in the quartz diorites, quartz monzonites and quartz porphyries (Fig. 7a–b).

The variation trends of major elements in the Nuri complex could be interpreted that the quartz porphyries and quartz monzonites were derived from fractional crystallization of the relatively primitive melts represented by quartz diorites. This interpretation is supported by the data of trace elements. Three types of rocks all exhibit fractionated REE patterns, while the contents of MREEs have a decreasing trend from quartz diorites to quartz monzonites and then to quartz porphyries (Fig. 5a). This could be caused by fractionation of hornblende, rather than garnet. Since the hornblende has higher partition coefficients for MREEs than HREEs (Table S4), low pressure crystallization involving hornblende would result in increasing $(La/Sm)_n$ ratios, but decreasing $(Dy/Yb)_n$ ratios with differentiation. In contrast, high pressure fractional crystallization of garnet would both cause increasing $(La/Sm)_n$ and $(Dy/Yb)_n$ ratios. The Nuri complex records an increase in $(La/Sm)_n$ ratios with increasing SiO_2 contents, whereas $(Dy/Yb)_n$ ratios show a slowly decreasing trend throughout the fractional crystallization process (Fig. 8a–b). These features are consistent with the fractional crystallization trend of hornblende (Davidson et al., 2007), rather than garnet fractionation (Macpherson et al., 2006). Additionally, the contents of compatible elements (Cr and Ni) decrease gradually from quartz diorites to quartz porphyries (Fig. 9c), also indicating the fractional crystallization of mafic minerals (e.g., hornblende and biotite).

Hornblende fractionation is seldom isolated and is typically accompanied by plagioclase removal (Moyen, 2009). As shown in Fig. 8c–e, Sr contents and Sr/Y, $(La/Yb)_n$ ratios gradually increase with increasing SiO_2 contents up to ca. 63 wt%, and subsequently decrease at higher SiO_2 contents, indicating that rocks in the Nuri complex underwent two stages of fractional crystallization process and plagioclase began to remove in the second stage. Since LREEs are incompatible both in hornblende and plagioclase (Table S4), fractionation of hornblende and

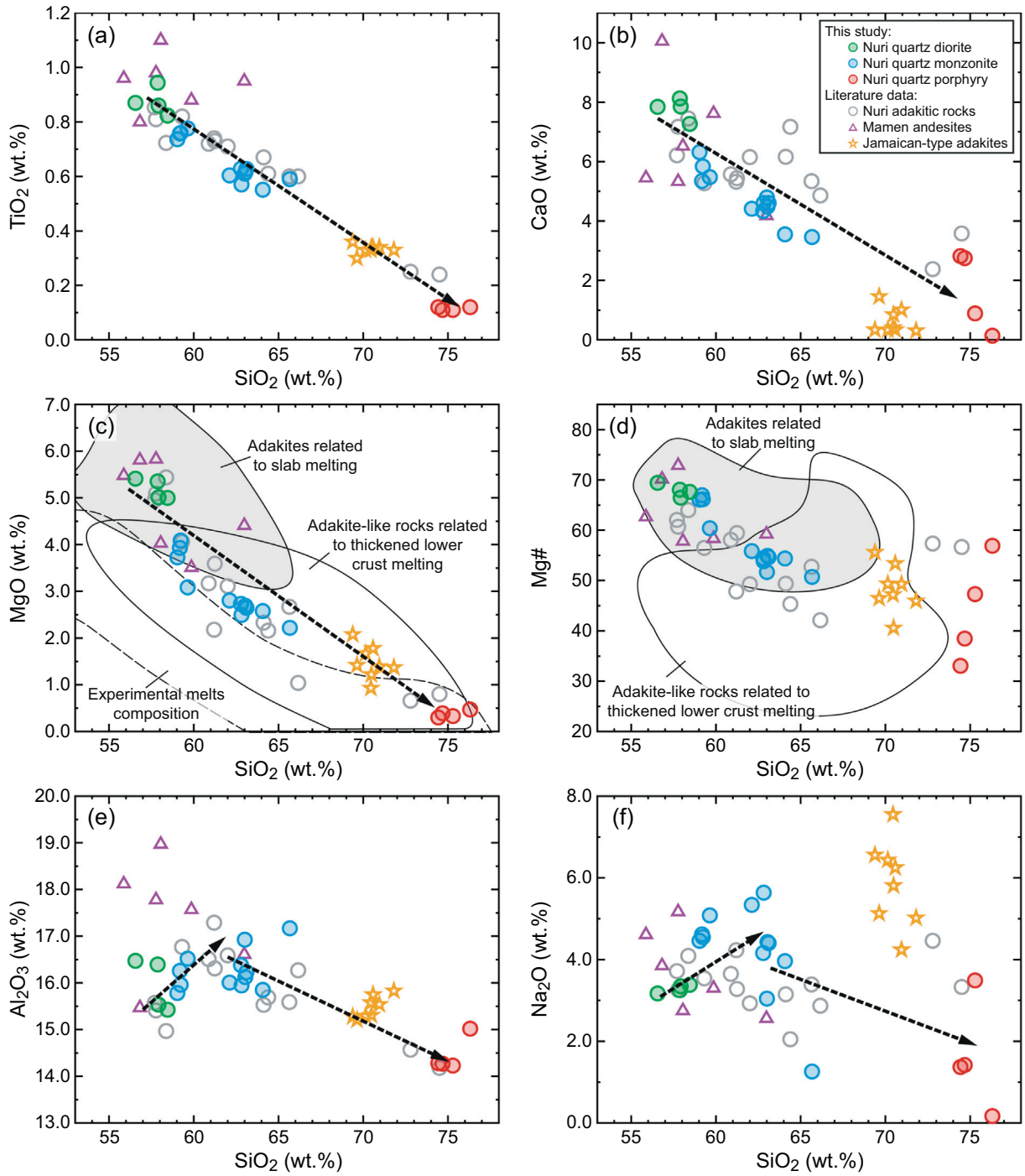

Fig. 6. (a) TiO_2, (b) CaO, (c) MgO, (d) Mg#, (e) Al_2O_3 and (f) Na_2O versus SiO_2 diagrams for the Nuri complex, southern Tibet. The fields of adakites related to slab melting and adakite–like rocks related to thickened lower crust melting are from Condie (2005), Zhu et al. (2009b) and Zheng et al. (2012b). The field of experimental melts is from Martin et al. (2005) and references therein. Data are from the same source as Fig. 4.

plagioclase should result in increasing LREEs contents from quartz diorites to quartz porphyries, which is opposite to the variation trends observed in the Nuri complex (Fig. 5a, 8f). This inconsistency implies that LREEs–rich accessory minerals (e.g., allanite and monazite) might also crystallize and segregate during the magmatic differentiation. In addition, more evolved magmas in the complex have normalized Ti and P data that show increasingly negative anomalies (Fig. 5b), which are likely to result from the fractional crystallization of Ti–bearing minerals and apatite.

Trace element modeling has been used to quantitatively estimate the degree of fractional crystallization and the type and proportion of crystallized minerals (details are shown in section 3.5), while the least fractionated sample of quartz diorites (NR11–30–2–3) has been assumed to represent the parental melt composition. The results show that the Nuri complex underwent ca. 20% fractional crystallization of 99% hornblende, 0.80% apatite, 0.14% zircon and 0.06% allanite in the first stage, and then underwent ca. 55% fractional crystallization of 42% plagioclase, 38% hornblende, 19% biotite, 0.60% apatite, 0.29%

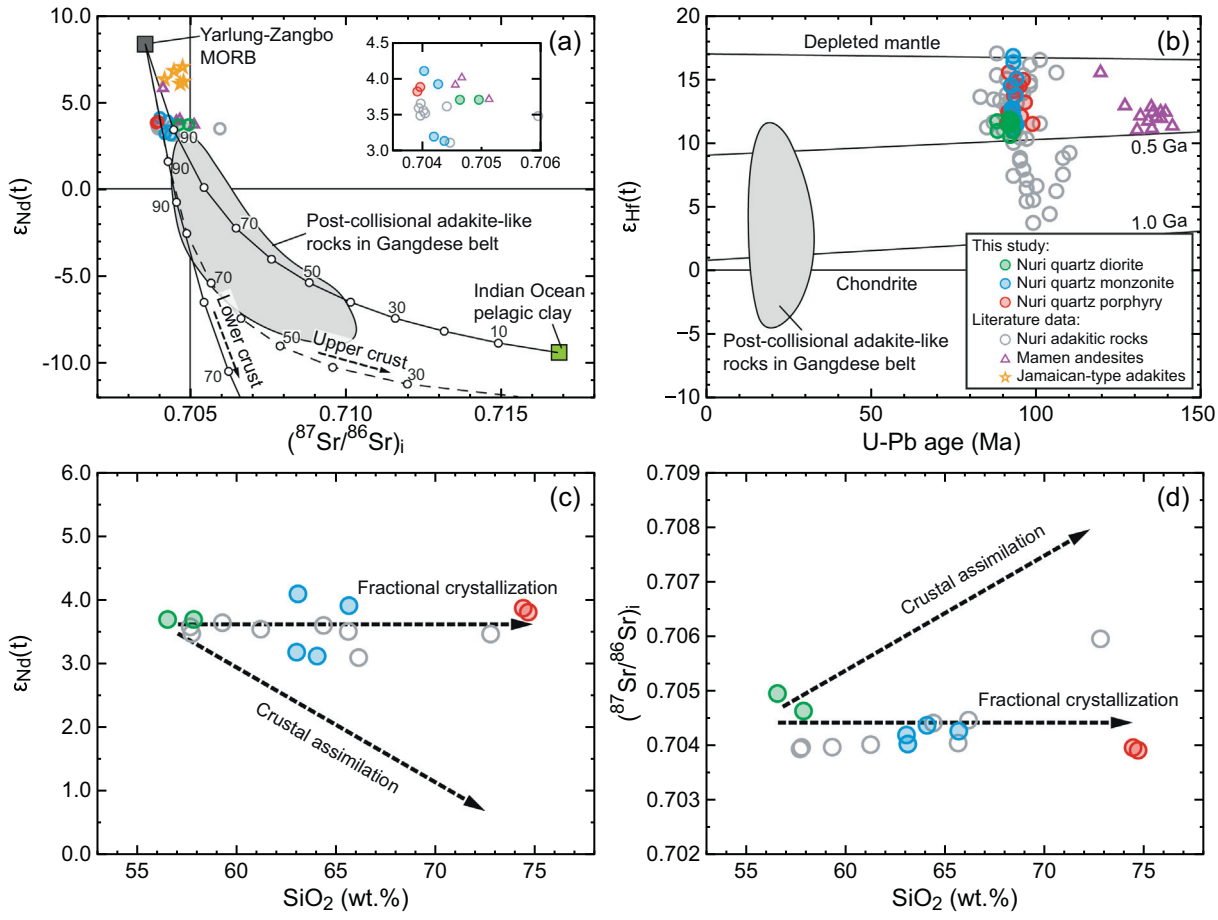

Fig. 7. (a) Whole–rock $\varepsilon_{Nd}(t)$ versus $(^{87}Sr/^{86}Sr)_i$, (b) $\varepsilon_{Hf}(t)$ versus U—Pb ages of zircons, (c) Whole–rock $\varepsilon_{Nd}(t)$ and (d) $(^{87}Sr/^{86}Sr)_i$ versus SiO_2 diagrams for the Nuri complex, southern Tibet. Data for Nuri adakitic rocks, Mamen andesites and Jamaican–type adakites are from the same source as Fig. 4. Data for Yarlung–Zangbo mid–ocean ridge basalt (MORB) is from Zhang et al. (2005). Data for Indian Ocean pelagic sediment is from Ben Othman et al. (1989). Data for the old lower crust and upper crust in Tibet are from Miller et al. (1999). The fields of post–collisional adakite–like rocks in Gangdese belt are from Hou et al. (2013, 2015) and references therein.

magnetite, 0.06% allanite, 0.03% zircon and 0.02% monazite in the second stage (Fig. 4c–d, 9, 10).

5.2.2. Magma source

As discussed above, the quartz diorites should represent the relatively primitive melts of the Nuri complex, while the complex underwent the fractional crystallization of hornblende, plagioclase, biotite and minor accessory minerals during the magmatic differentiation. Therefore, the quartz diorites can be used to provide some constraints on source region of the Nuri complex. The quartz diorites show typical adakitic features with high Sr/Y and $(La/Yb)_n$ ratios (Fig. 4c–d). Though various petrogenetic models have been proposed (e.g., Castillo et al., 1999; Defant and Drummond, 1990; Hastie et al., 2010a; Hou et al., 2004; Macpherson et al., 2006; Martin et al., 2005; Rapp et al., 1999; Streck et al., 2007; Xu et al., 2002), the following several lines of evidence suggest that quartz diorites were most probably originated from partial melting of subducted Neo–Tethyan oceanic crust.

Quartz diorites are characterized by high Mg# values (66–69), and MgO, Cr, and Ni contents (5.00–5.41 wt%, 138–159 ppm, 65.9–96.8 ppm, respectively), which could preclude the possibility that they were derived from partial melting of a thickened mafic lower crust underneath southern Tibet (Fig. 6c–d, 9c; e.g., Zheng et al., 2012a, 2012b; Guan et al., 2012; Hou et al., 2013). The features of high MgO, Cr and Ni contents are commonly regarded as the results of interaction between ascending melts and overlying mantle wedge, while this process would not change the features of melts as recorded by other trace elements (e.g., REEs, Sr and Y) (Rapp et al., 1999). Such scenario could occur either in subduction settings or regions where the lower part of lower crust may have delaminated (e.g., Rapp et al., 1999; Wang et al., 2007; Xu et al., 2002; Zhu et al., 2009b). Delaminated lower crust model would require the existence of thickened continental crust (Wang et al., 2007; Xu et al., 2002). However, the temporal variations in crustal thickness estimated by whole–rock $(La/Yb)_n$ ratios show that the Gangdese belt did not evidently thicken until 70–60 Ma (Zhu et al., 2017), indicating that delaminated lower crust model cannot be used to explain the geochemical features of quartz diorites. Thus, the remaining candidate is the slab melting model. Typically, it would not be easy for slab melts to reach the surface because they would quickly freeze in the peridotite mantle constrained by experimental investigation (Yaxley and Green, 1998). Only at high slab melt/peridotite ratios, the slab–derived melts can successfully ascent through the overlying mantle wedge (Rapp et al., 1999). HSA and LSA were proposed to represent the subducted slab melts after interacted with overlying mantle wedge and the adakitic melts generated by partial melting of mantle wedge metasomatised by felsic slab melts, respectively (Martin et al., 2005). In this study, quartz diorites all plot within the HSA fields in the discriminant diagrams (Fig. 11), indicating that these rocks should be derived from partial melting of subducted oceanic crust and then interact with the mantle wedge during their ascent. This conclusion is further supported by Sr–Nd–Hf isotopic data.

The Oligocene–Miocenepost–collisionaladakite–like rocks in Gangdese belt have been taken as typical melts derived from the thickened mafic lower crust (e.g., Hou et al., 2004, 2013; Zheng et al., 2012a, 2012b). Significant differences in whole–rock$(^{87}Sr/^{86}Sr)_i$ and $\varepsilon_{Nd}(t)$

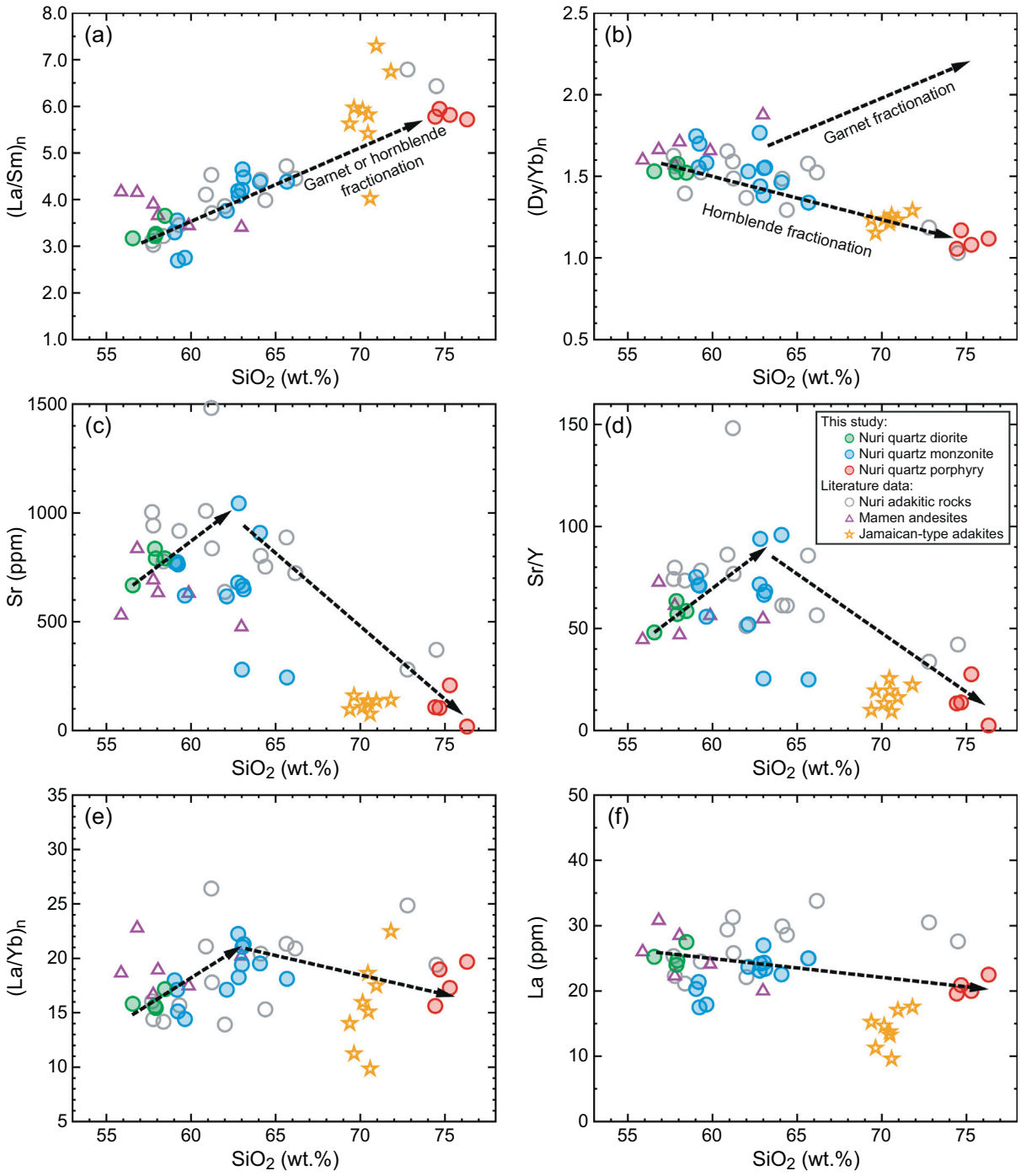

Fig. 8. (a) $(La/Sm)_n$, (b) $(Dy/Yb)_n$, (c) Sr, (d) Sr/Y, (e) $(La/Yb)_n$ and (f) La versus SiO_2 diagrams for the Nuri complex, southern Tibet. Chondrite and primitive mantle normalizing values are from Sun and McDonough (1989). Data are from the same source as Fig. 4.

values, and zircon $\varepsilon_{Hf}(t)$ values from these post–collisionaladakite–like rocks indicate that the Nuri quartz diorites could not be derived from thickened lower crust melting (Fig. 7). In contrast, not only the relatively depleted isotopic features of quartz diorites, but also high MgO, Cr, Ni contents, are comparable to the Mamen adakites (ca. 136.5 Ma) in the same area (Fig. 6c–d, 7a–b, 9c). The Mamen adakites have been considered to be generated by partial melting of the subducted Neo–Tethyan oceanic crust and subsequently interact with overlying mantle wedge (Zhu et al., 2009b). Therefore, the Nuri quartz diorites should have similar source region to that of the Mamen adakites.

Besides the subducted oceanic crust, both slab–derived fluids and subducted sediments might have also contributed materials to the generation of the Nuri complex. Since slab–derived fluids are commonly enriched in LILEs (Guo et al., 2005), variable Ba/La ratios coupled with a relatively narrow range of Nb/Y ratios represent the contributions of slab–derived fluids (Fig. 12a). Additionally, present–day arc magmas with the involvement of large amounts of subducted sediments commonly have Th/Yb ratios ≥2 because of the high Th contents of the melts derived from subducted sediments (Hawkesworth et al., 1997a; Nebel et al., 2007). Therefore, the high Th/Yb ratios combined with a liner trend in the Th/Yb versus Th/Sm diagram indicate the contribution of subducted sediments to the development of the Nuri complex (Fig. 12b). Whole–rock $(^{87}Sr/^{86}Sr)_i$ and $\varepsilon_{Nd}(t)$ values of the complex fall on a mixing line between

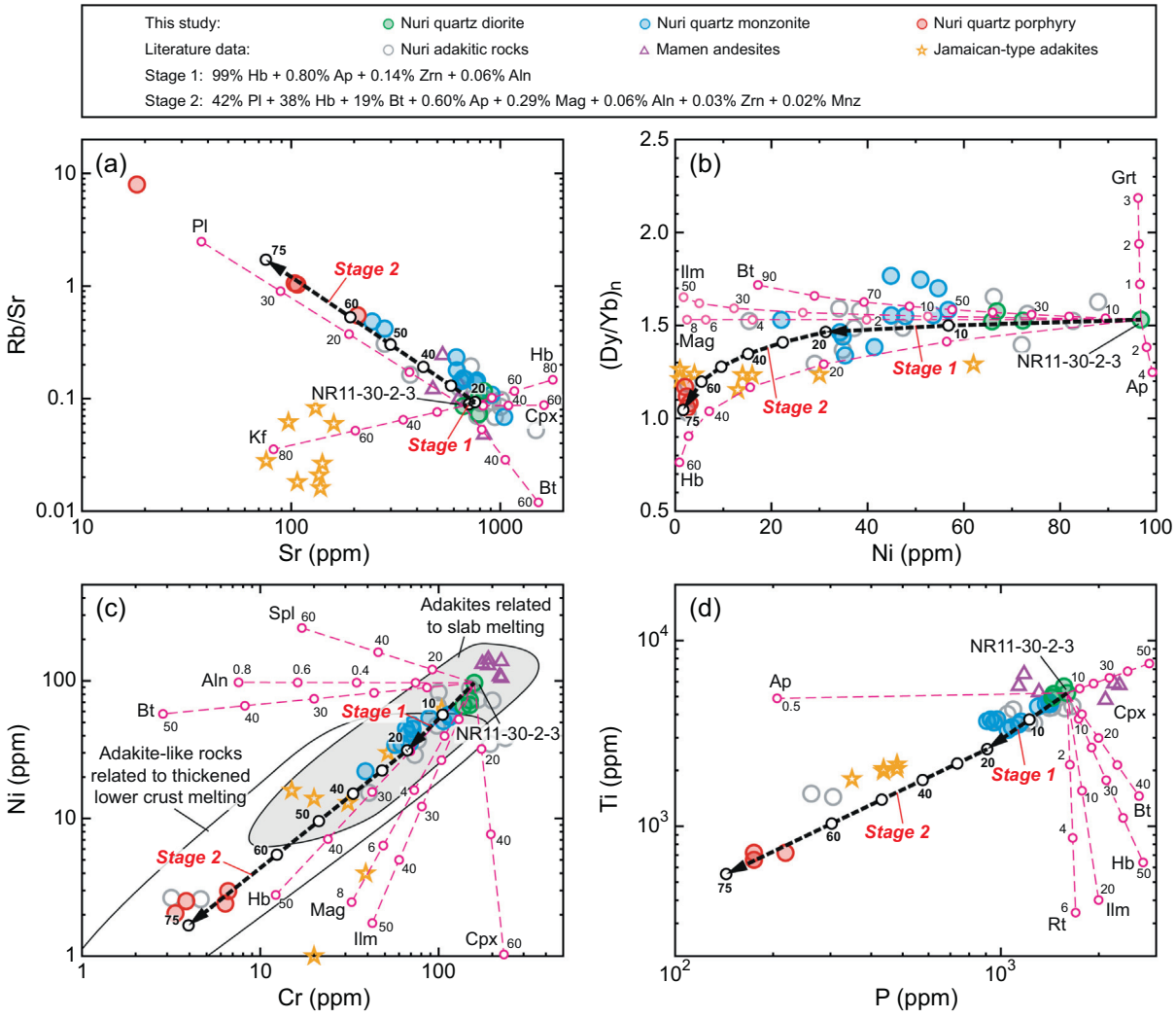

Fig. 9. (a) Rb/Sr versus Sr; (b) $(Dy/Yb)_n$ versus Ni; (c) Ni versus Cr and (d) Ti versus P diagrams showing fractional crystallization trends in the Nuri complex. The fields of adakites related to slab melting and adakite–like rocks related to thickened lower crust melting are from Zheng et al. (2012b). Mineral/melt partition coefficients are listed in Table S4. Abbreviations: Aln = allanite, Ap = apatite, Bt = biotite, Cpx = clinopyroxene, Grt = garnet, Hb = hornblende, Ilm = ilmenite, Kf = K–feldspar, Mag = magnetite, Pl = plagioclase, Rt = rutile, Spl = spinel.

Yarlung–Zangbomid–ocean ridge basalts (MORB) (Zhang et al., 2005) and Indian ocean pelagic sediments (Ben Othman et al., 1989) (Fig. 7a), indicating that the contribution of subducted sediments is less than ca. 10%. No evidently $(^{87}Sr/^{86}Sr)_i$ and $\varepsilon_{Nd}(t)$ values changing with the increasing SiO_2 contents suggests that magmas in the Nuri complex were not significantly assimilated by the ancient crustal materials during their ascent (Fig. 7c–d).

5.3. Implication for the JTA–like geochemical features

Studying modern adakites would be useful in understanding the petrogenesis of Archaean TTGs and the origin of continental crust in the early Earth (Castillo, 2012, and references therein). For instance, since Phanerozoic adakites and Middle–Late Archean TTGs (3.5–2.5 Ga) show similar geochemical compositions, these two types of rocks are commonly considered to be generated by similar processes (i.e., partial melting of subducted oceanic slabs) (e.g., Martin, 1999; Martin et al., 2005; Smithies et al., 2003, 2009). However, the geochemical compositions of TTGs have changed through Archaean times, while the Early Archean TTGs (> 3.5 Ga) exhibit lower Sr contents and Sr/Y ratios, as well as lower MgO, Cr and Ni contents than Middle–Late Archean TTGs (Martin et al., 2005; Martin and Moyen, 2002; Smithies et al., 2003). No modern analogues of Early Archean TTGs had been discovered until Hastie et al. (2010a, 2010b) reported that the Phanerozoic Newcastle rhyodacites from eastern Jamaica. Newcastle rhyodacites have adakitic major and trace element compositions with high SiO_2, Al_2O_3 contents and high $(La/Yb)_n$ ratios as well as low HREEs and Y contents, while they also have several geochemical features which are different from typical adakites but are similar to Early Archean TTGs, like lower MgO, Cr, Ni, Sr contents and Sr/Y ratios. Therefore, these rhyodacites were defined as a new adakite subgroup, named as "Jamaican–type adakites" (JTAs) (Hastie et al., 2010a).

Subduction of oceanic plateau has been proposed to account for the petrogenesis of JTAs. Low contents of MgO, Cr and Ni have been explained by the partial melting of subducted oceanic plateau crust whereby the slab melts did not interact with mantle wedge (Hastie et al., 2010a, 2010b) or might have limited interaction with a thin and/or discontinuous mantle wedge but followed by small amounts of hornblende fractionation (Hastie et al., 2015). Low Sr contents and Sr/Y ratios have been interpreted as the results of residual plagioclase (Hastie et al., 2010a, 2010b, 2015). Thus, Hastie et al. (2010b, 2015) suggested that Early Archean TTGs and the first continents were generated by the subduction of oceanic plateau–like oceanic crust. New high P–T experiments also demonstrated that tonalite melts similar to Early Archean TTGs in composition could be generated by partial melting of primitive oceanic plateau material mixed with slab–derived aqueous fluids (Hastie et al., 2016).

In this study, Nuri quartz porphyries and JTAs are similar in overall compositions with a few differences. The main differences are that

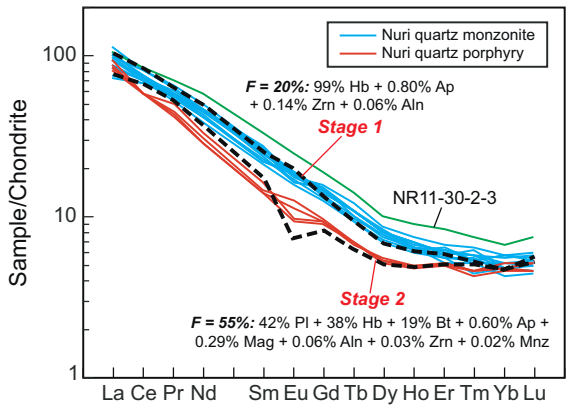

Fig. 10. Modeled REE patterns with quantitative fractionated phase combinations. The assumed parental melt composition was represented by the least fractionated sample of quartz diorites (NR11–30–2–3). Mineral/melt partition coefficients are listed in Table S4. Abbreviations: Aln = allanite, Ap = apatite, Bt = biotite, Hb = hornblende, Mag = magnetite, Mnz = monazite, Pl = plagioclase, Zrn = zircon.

the JTAs are sodic with low K_2O/Na_2O ratios and Rb contents, while not only the quartz porphyries but total complex are potassic and have high Rb contents (Fig. 4a, 5b). This might result from the more contributions of subducted sediments to the Nuri complex than the JTAs, which is supported by the Sr—Nd isotopic data (Fig. 7a). Subducted sediments can release significant amounts of K and Rb when the micas breakdown, since mica is the primary hydrous phase in sedimentary systems and controls partitioning behavior of K and Rb (Johnson and Plank, 2000). Additionally, deep sea sediments which contain remarkably high contents of REEs were recently discovered in Indian Ocean (Yasukawa et al., 2014). The involvement of this kind of sediments may account for the relatively higher total REEs contents of the Nuri complex (Fig. 5a). Although some compositional differences exist, Nuri quartz porphyries are similar to JTAs in key geochemical features that are used to distinguish between JTAs and typical adakites, and also between Early Archean TTGs and Middle–Late Archean TTGs. For instance, the fractionated REE patterns with low MREEs, HREEs and Y contents (e.g., Yb, 0.79–0.90 ppm; Y, 7.37–8.04 ppm) but relatively high $(La/Yb)_n$ ratios (15.6–19.7), as well as the relatively low Sr contents (18.3–208 ppm) and Sr/Y ratios (2.48–27.59) of the quartz porphyries are all comparable to the JTAs. Both of these two types of rocks dominantly plot below the field of adakites in the Sr/Y versus Y diagram (Fig. 4c). Additionally, quartz porphyries also have low contents of MgO (0.30–0.47 wt%) and compatible elements (e.g., Cr, 3.34–6.60 ppm; Ni, 2.05–2.97 ppm). As discussed above, however, these features were originated from the Nuri quartz diorites by frac-

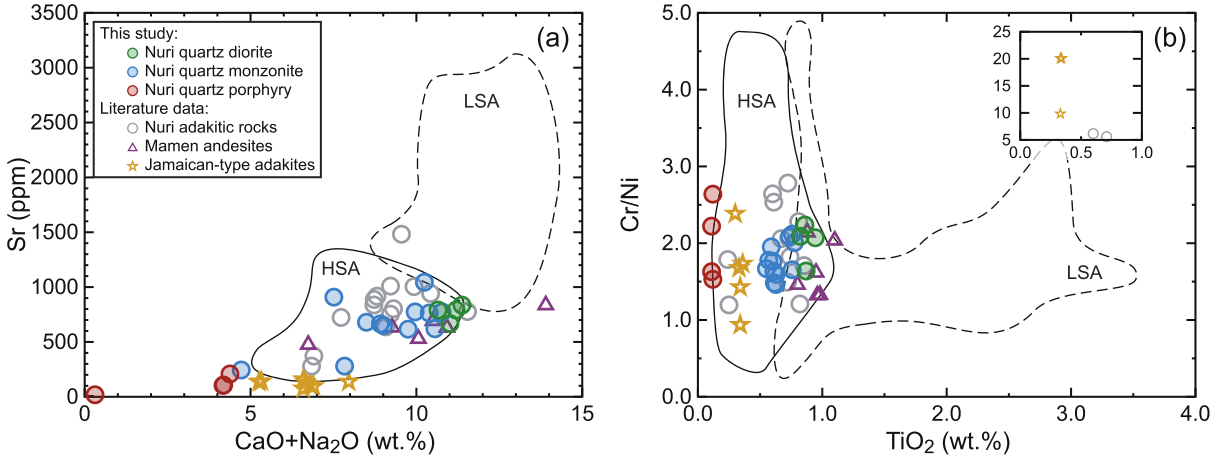

Fig. 11. (a) Sr versus CaO + Na_2O and (b) Cr/Ni versus TiO_2 diagrams for the Nuri complex, southern Tibet. The fields of high-SiO_2 adakitic rocks (HSA) and low-SiO_2 adakitic rocks (LSA) are from Martin et al. (2005). Data are from the same source as Fig. 4.

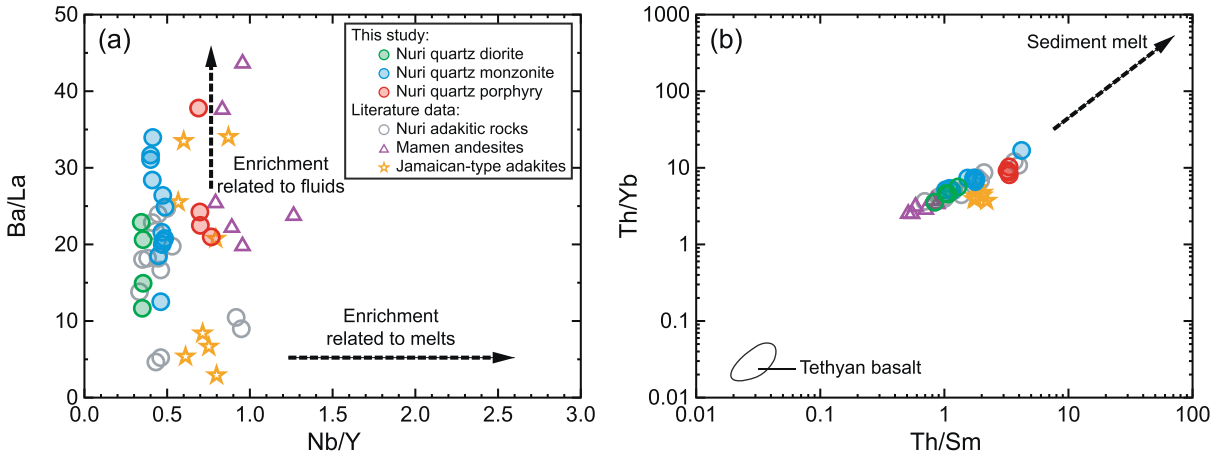

Fig. 12. (a) Ba/La versus Nb/Y, and (b) Th/Yb versus Th/Sm diagrams for the Nuri complex, southern Tibet. The field of Tethyan basalts is from Zhu et al. (2009b). Data are from the same source as Fig. 4.

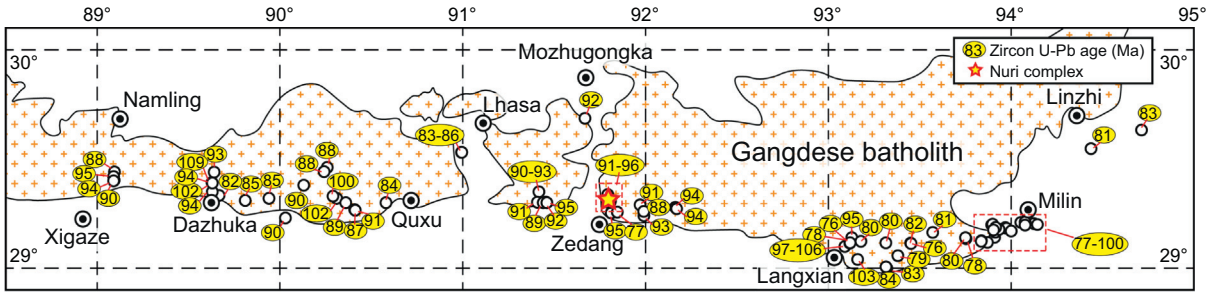

Fig. 13. Simplified geologic map showing the distribution of Late Cretaceous igneous rocks and their ages in Gangdese belt (modified from Ma et al., 2015). Data for the Late Cretaceous igneous rocks are listed in Table S5.

tional crystallization. Fractionation of hornblende, biotite, with minor magnetite and allanite would result in low MgO, Cr and Ni contents of the quartz porphyries, while plagioclase fractionation would lead to low Sr contents and Sr/Y ratios (Fig. 4c–d, 9, 10). Therefore, partial melting of subducted oceanic plateau crust leaving a residue of hornblende, garnet and plagioclase could be not the only way to develop rocks with JTA–like geochemical features. This conclusion is consistent with a previously study on the JTA–like rhyodacites in the northeastern Japan arc, which might be generated by the fractional crystallization of plagioclase, orthopyroxene, clinopyroxene, hornblende, garnet, titanomagnetite and minor apatite from normal arc magmas (Shuto et al., 2013).

5.4. Late cretaceous magmatic "flare–up" in Gangdese belt

According to previously published zircon U—Pb age data, a magmatic "flare–up" occurred in the Gangdese belt in the period of Late Cretaceous (109–76 Ma). These magmas contain various rock types ranging from gabbro to granite, and include both normal arc magmas and adakitic rocks (e.g., Ma et al., 2013a, 2013b, 2013c, 2015; Wen et al., 2008a, 2008b; Xu et al., 2015; Zhang et al., 2010; Zheng et al., 2014). They are distributed along a narrow E–W trending belt extending from Xigaze to Linzhi (Fig. 13).

Large–scale magmatism usually is a response to a certain tectono–magmatic event. Nevertheless, the triggering mechanism for the Late Cretaceous magmatic "flare–up" remains controversial. Several subduction–related geodynamic models have been proposed, including (1) mid–ocean ridge subduction (Guo et al., 2013; Zhang et al., 2010; Zheng et al., 2014), (2) low–angle or flat oceanic slab subduction (Wen et al., 2008a, 2008b), and (3) roll–back of subducted oceanic slab (Chen et al., 2015; Ma et al., 2013a, 2013b, 2013c; Xu et al., 2015). Flat subduction of the oceanic slab would squeeze out the mantle wedge, which is inconsistent with the widespread contemporary mantle–derived mafic rocks from Xigaze to Linzhi (Ma et al., 2013a, 2013b, 2015; Xu et al., 2015). Slab roll–back model would require that magmatism in Gangdese belt began in the north and propagated southwards, however, the Late Cretaceous igneous rocks do not show any age trend in the distribution (Fig. 13). Therefore, mid–ocean ridge subduction is the most likely geodynamic model. This is supported by high temperature charnockitic and noritic magmatism (Ma et al., 2013a, 2013c; Zhang et al., 2010) and high temperature granulite–facies metamorphism (Guo et al., 2013; Wang et al., 2009), which implies a significantly high heat flux during the Late Cretaceous. Especially, the fore–arc region is typically a setting for low temperature metamorphism (Groome and Thorkelson, 2009), but in Gangdese belt, both arc igneous rocks and fore–arc sedimentary rocks underwent Late Cretaceous high temperature granulite–facies metamorphism, indicating that anomalously high heat flowed through the slab window beneath the arc and fore–arc region due to the Neo–Tethyanmid–ocean ridge subduction (Guo et al., 2013). Besides the upwelling of hot asthenospheric mantle, the basaltic oceanic crust along the edges of mid–ocean ridge was mostly young and hot, which would also significantly increase temperatures in the subduction zone (Iwamori, 2000). The large amounts of heat not only resulted in the partial melting of the overlying mantle wedge to form Late Cretaceous normal arc magmas in Gangdese belt, but also triggered the partial melting of the subducted oceanic crust to form the adakites.

6. Conclusions

1. The Nuri complex was emplaced in the Late Cretaceous (93.5–92.1 Ma) and derived from partial melting of subducted Neo–Tethyan oceanic crust with the involvement of subducted sediments and slab–derived fluids. Subsequently, the complex underwent metasomatic reaction with mantle wedge peridotite and fractional crystallization process. The quartz monzonites and quartz porphyries were evolved from the quartz diorites through the fractional crystallization of hornblende with minor apatite, zircon and allanite in the first stage and of plagioclase, hornblende, biotite, with minor apatite, magnetite, allanite, zircon and monazite in the second stage.
2. The JTA–like geochemical features can be generated by fractional crystallization from the adakites derived from partial melting of subducted slab. Low MgO, Cr and Ni contents could be the results of fractionation of hornblende, biotite, with minor magnetite and allanite, while low Sr contents and Sr/Y ratios could be mainly controlled by plagioclase fractionation.
3. In Gangdese belt, Late Cretaceous magmatic "flare–up" might be triggered by subduction of the Neo–Tethyanmid–ocean ridge.

Supplementary data to this article can be found online at https://doi.org/10.1016/j.lithos.2018.09.031.

Acknowledgments

This work was funded by the National Key Research and Development Project of China(2016YFC0600310), the Ministry of Science and Technology of China (973 Project 2015CB452600, 2011CB4031006), the Program of the China Geological Survey(DD20160024–07, DD20179172), NSFC(41472076, 41872083), IGCP/SIDA–600, and the Fundamental Research Funds for the Central Universities(53200859424). We thank Qiang Fu for his assistance in the field and Song Zhang for helping with zircon U—Pb dating and Lu—Hf isotopic analyses. We are most grateful to Dr. Alan Hastie and an anonymous reviewer for critical and constructive reviews of this manuscript. This is CUGB petro-geochemical contribution NO. PGC-2015034 (E7110214).

References

Andersen, T., 2002. Correction of common lead in U–Pb analyses that do not report ^{204}Pb. Chem. Geol. 192, 59–79.

Ben Othman, D., White, W.M., Patchett, J., 1989. The geochemistry of marine sediments, island arc magma genesis, and crust–mantle recycling. Earth Planet. Sci. Lett. 94, 1–21.

Blichert Toft, J., Albarède, F., 1997. The Lu–Hf isotope geochemistry of chondrites and the evolution of the mantle–crust system. Earth Planet. Sci. Lett. 148, 243–258.
Castillo, P.R., 2012. Adakite petrogenesis. Lithos 134–135, 304–316.
Castillo, P.R., Janney, P.E., Solidum, R.U., 1999. Petrology and geochemistry of Camiguin Island, southern Philippines: insights to the source of adakites and other lavas in a complex arc setting. Contrib. Mineral. Petrol. 134, 33–51.
Chen, L., Qin, K.Z., Li, G.M., Li, J.X., Xiao, B., Zhao, J.X., Fan, X., 2015. Zircon U–Pb ages, geochemistry, and Sr–Nd–Pb–Hf isotopes of the Nuri intrusive rocks in the Gangdese area, southern Tibet: Constraints on timing, petrogenesis, and tectonic transformation. Lithos 212 (215), 379–396.
Chung, S.L., Liu, D.Y., Ji, J.Q., Chu, M.F., Lee, H.Y., Wen, D.J., Lo, C.H., Lee, T.Y., Qian, Q., Zhang, Q., 2003. Adakites from continental collision zones: Melting of thickened lower crust beneath southern Tibet. Geology 31, 1021–1024.
Condie, K.C., 2005. TTGs and adakites: are they both slab melts? Lithos 80, 33–44.
Davidson, J., Turner, S., Handley, H., Macpherson, C., Dosseto, A., 2007. Amphibole "sponge" in arc crust? Geology 35, 787–790.
Defant, M.J., Drummond, M.S., 1990. Derivation of some modern arc magmas by melting of young subducted lithosphere. Nature 347, 662–665.
Dong, X., Zhang, Z.M., Santosh, M., 2010. Zircon U–Pb Chronology of the Nyingtri Group, Southern Lhasa Terrane, Tibetan Plateau: Implications for Grenvillian and Pan–African Provenance and Mesozoic–Cenozoic Metamorphism. The Journal of Geology 118, 677–690.
Griffin, W.L., Pearson, N.J., Belousova, E., Jackson, S.E., van Achterbergh, E., O'Reilly, S.Y., Shee, S.R., 2000. The Hf isotope composition of cratonic mantle: LAM–MC–ICPMS analysis of zircon megacrysts in kimberlites. Geochim. Cosmochim. Acta 64, 133–147.
Griffin, W.L., Wang, X., Jackson, S.E., Pearson, N.J., O'Reilly, S.Y., Xu, X., Zhou, X., 2002. Zircon chemistry and magma mixing, SEChina: *In-situ* analysis of Hf isotopes, Tonglu and Pingtan igneous complexes. Lithos 61, 237–269.
Groome, W.G., Thorkelson, D.J., 2009. The three-dimensionalthermo-mechanical signature of ridge subduction and slab window migration. Tectonophysics 464, 70–83.
Guan, Q., Zhu, D.C., Zhao, Z.D., Dong, G.C., Zhang, L.L., Li, X.W., Liu, M., Mo, X.X., Liu, Y.S., Yuan, H.L., 2012. Crustal thickening prior to 38 Ma in southern Tibet: evidence from lower crust–derived adakitic magmatism in the Gangdese Batholith. Gondwana Res. 21, 88–99.
Guo, Z.F., Hertogen, J., Liu, J.Q., Pasteels, P., Boven, A., Punzalan, L., He, H.Y., Luo, X.J., Zhang, W.H., 2005. Potassic Magmatism in Western Sichuan and Yunnan Provinces, SE Tibet, China: Petrological and Geochemical Constraints on Petrogenesis. J. Petrol. 46, 33–78.
Guo, F., Nakamuru, E., Fan, W., Kobayoshi, K., Li, C., 2007. Generation of Palaeocene Adakitic Andesites by Magma Mixing; Yanji Area, NEChina. J. Petrol. 48, 661–692.
Guo, L., Zhang, H.F., Harris, N., Pan, F.B., Xu, W.C., 2013. Late cretaceous (81 Ma) high–temperature metamorphism in the southeastern Lhasa terrane: Implication for the Neo–Tethys Ocean ridge subduction. Tectonophysics 608, 112–126.
Hastie, A.R., Kerr, A.C., McDonald, I., Mitchell, S.F., Pearce, J.A., Millar, I.L., Barfod, D., Mark, D.F., 2010a. Geochronology, geochemistry and petrogenesis of rhyodacite lavas in eastern Jamaica: a new adakite subgroup analogous to early Archaean continental crust? Chem. Geol. 276, 344–359.
Hastie, A.R., Kerr, A.C., McDonald, I., Mitchell, S.F., Pearce, J.A., Wolstencroft, M., Millar, I.L., 2010b. Do Cenozoic analogues support a plate tectonic origin for Earth's earliest continental crust? Geology 38, 495–498.
Hastie, A.R., Fitton, J.G., Mitchell, S.F., Neill, I., Nowell, G.M., Millar, I.L., 2015. Can Fractional Crystallization, Mixing and Assimilation Processes be responsible for Jamaican–type Adakites? Implications for Generating Eoarchaean Continental Crust. J. Petrol. 56, 1251–1284.
Hastie, A.R., Fitton, J.G., Bromiley, G.D., Butler, I.B., Odling, N.W.A., 2016. The origin of Earth's first continents and the onset of plate tectonics. Geology 44, 855–858.
Hawkesworth, C.J., Turner, S., Peate, D., McDermott, F., van Calsteren, P., 1997a. Elemental U and Th variations in island arc rocks: implications for U–series isotopes. Chem. Geol. 139, 207–221.
Hoskin, P.W.O., Schaltegger, U., 2003. The composition of zircon and igneous and metamorphic petrogenesis. Rev. Mineral. Geochem. 53, 27–62.
Hou, Z.Q., Gao, Y.F., Qu, X.M., Rui, Z.Y., Mo, X.X., 2004. Origin of adakitic intrusives generated during mid–Mioceneeast–west extension in southern Tibet. Earth Planet. Sci. Lett. 220, 139–155.
Hou, Z.Q., Zheng, Y.C., Yang, Z.M., Rui, Z.Y., Zhao, Z.D., Jiang, S.H., Qu, X.M., Sun, Q.Z., 2013. Contribution of mantle components within juvenile lower–crust to collisional zone porphyry Cu systems in Tibet. Mineral. Deposita 48, 173–192.
Hou, Z.Q., Duan, L.F., Lu, Y.J., Zheng, Y.C., Zhu, D.C., Yang, Z.M., Yang, Z.S., Wang, B.D., Pei, Y.R., Zhao, Z.D., 2015. Lithospheric Architecture of the Lhasa Terrane and its Control on Ore Deposits in the Himalayan–Tibetan Orogen. Econ. Geol. 110, 1541–1575.
Iwamori, H., 2000. Thermal effects of ridge subduction and its implications for the origin of granitic batholith and paired metamorphic belts. Earth Planet. Sci. Lett. 181, 131–144.
Ji, W.Q., Wu, F.Y., Chung, S.L., Li, J.X., Liu, C.Z., 2009. Zircon U–Pb geochronology and Hf isotopic constraints on petrogenesis of the Gangdese batholith, southern Tibet. Chem. Geol. 262, 229–245.
Johnson, M.C., Plank, T., 2000. Dehydration and melting experiments constrain the fate of subducted sediments. Geochem. Geophys. Geosyst. 1.
Kang, Z.Q., Xu, J.F., Wilde, S.A., Feng, Z.H., Chen, J.L., Wang, B.D., Fu, W.C., Pan, H.B., 2014. Geochronology and geochemistry of the Sangri Group Volcanic Rocks, Southern Lhasa Terrane: Implications for the early subduction history of the Neo–Tethys and Gangdese Magmatic Arc. Lithos 200–201, 157–168.
Kay, R., 1978. Aleutian magnesian andesites: melts from subducted Pacific Ocean crust. J. Volcanol. Geotherm. Res. 4, 117–132.
Liu, Y.S., Gao, S., Hu, Z.C., Gao, C.G., Zong, K.Q., Wang, D.B., 2010. Continental and Oceanic Crust Recycling–inducedMelt–Peridotite Interactions in the Trans–NorthChina Orogen: U–Pb Dating, Hf Isotopes and Trace elements in Zircons from Mantle Xenoliths. J. Petrol. 51, 537–571.
Ludwig, K., 2003. Isoplot V. 3.0: A Geochronological Toolkit for Microsoft Excel. Berkeley Geochronology Center Special Publication.
Ma, L., Wang, Q., Li, Z.X., Wyman, D.A., Jiang, Z.Q., Yang, J.H., Gou, G.N., Guo, H.F., 2013a. Early late cretaceous (ca. 93 Ma) norites and hornblendites in the Milin area, eastern Gangdese: Lithosphere–asthenosphere interaction during slab roll–back and an insight into early late cretaceous (ca. 100–80 Ma) magmatic "flare–up" in southern Lhasa (Tibet). Lithos 172–173, 17–30.
Ma, L., Wang, Q., Wyman, D.A., Jiang, Z.Q., Yang, J.H., Li, Q.L., Gou, G.N., Guo, H.F., 2013b. Late cretaceous crustal growth in the Gangdese area, southern Tibet: Petrological and Sr–Nd–Hf–O isotopic evidence from Zhengga diorite–gabbro. Chem. Geol. 349–350, 54–70.
Ma, L., Wang, Q., Wyman, D.A., Li, Z.X., Jiang, Z.Q., Yang, J.H., Gou, G.N., Guo, H.F., 2013c. Late cretaceous (100–89 Ma) magnesian charnockites with adakitic affinities in the Milin area, eastern Gangdese: Partial melting of subducted oceanic crust and implications for crustal growth in southern Tibet. Lithos 175–176, 315–332.
Ma, L., Wang, Q., Wyman, D.A., Jiang, Z.Q., Wu, F.Y., Li, X.H., Yang, J.H., Gou, G.N., Guo, H.F., 2015. Late cretaceous back-arc extension and arc system evolution in the Gangdese area, southern Tibet: Geochronological, petrological, and Sr-Nd-Hf-O isotopic evidence from Dagze diabases. J. Geophys. Res. 120, 6159–6181.
Macpherson, C.G., Dreher, S.T., Thirlwall, M.F., 2006. Adakites without slab melting: High pressure differentiation of island arc magma, Mindanao, the Philippines. Earth Planet. Sci. Lett. 243, 581–593.
Martin, H., 1999. Adakitic magmas: modern analogues of Archaean granitoids. Lithos 46, 411–429.
Martin, H., Moyen, J.–.F., 2002. Secular changes in tonalite–trondhjemite–granodiorite composition as markers of the progressive cooling of Earth. Geology 30, 319–322.
Martin, H., Smithies, R.H., Rapp, R., Moyen, J.F., Champion, D., 2005. An overview of adakite, tonalite–trondhjemite–granodiorite (TTG), and sanukitoid: relationships and some implications for crustal evolution. Lithos 79, 1–24.
Meng, J., Wang, C.S., Zhao, X.X., Coe, R., Li, Y.L., Finn, D., 2012. India-Asia collision was at 24°N and 50 Ma: palaeomagnetic proof from southernmost Asia. Sci. Rep. 2, 925.
Miller, C., Schuster, R., Klötzli, U., Frank, W., Purtscheller, F., 1999. Post–collisional potassic and ultrapotassic magmatism in SW Tibet: geochemical and Sr–Nd–Pb–O isotopic constraints for mantle source characteristics and petrogenesis. J. Petrol. 40, 1399–1424.
Moyen, J.F., 2009. High Sr/Y and La/Yb ratios: the meaning of the "adakitic signature". Lithos 112, 556–574.
Nebel, O., Münker, C., Nebel–Jacobsen, Y.J., Kleine, T., Mezger, K., Mortimer, N., 2007. Hf–Nd–Pb isotope evidence from Permian arc rocks for the long–term presence of the Indian–Pacific mantle boundary in the SW Pacific. Earth Planet. Sci. Lett. 254, 377–392.
Pan, G.T., Ding, J., Yao, D.S., Wang, L.Q., 2004. Guidebook of 1:1,500,000 geologic map of the Qinghai–Xizang (Tibet) plateau and adjacent areas 1–148.
Peccerillo, A., Taylor, S.R., 1976. Geochemistry of eocene calc–alkaline volcanic rocks from the Kastamonu area, Northern Turkey. Contrib. Mineral. Petrol. 58, 63–81.
Rapp, R.P., Shimizu, N., Norman, M.D., Applegate, G.S., 1999. Reaction between slab–derived melts and peridotite in the mantle wedge: experimental constraints at 3.8 GPa. Chem. Geol. 160, 335–356.
Shuto, K., Sato, M., Kawabata, H., Osanai, Y., Nakano, N., Yashima, R., 2013. Petrogenesis of Middle Miocene Primitive Basalt, Andesite and Garnet–bearing Adakitic Rhyodacite from the Ryozen Formation: Implications for the Tectono–magmatic Evolution of the NEJapan Arc. J. Petrol. 54, 2413–2454.
Smithies, R.H., 2000. The Archaean tonalite–trondhjemite–granodiorite (TTG) series is not an analogue of Cenozoic adakite. Earth Planet. Sci. Lett. 182, 115–125.
Smithies, R.H., Champion, D.C., Cassidy, K.F., 2003. Formation of Earth's early Archaean continental crust. Precambrian Res. 127, 89–101.
Smithies, R.H., Champion, D.C., Van Kranendonk, M.J., 2009. Formation of Paleoarchean continental crust through infracrustal melting of enriched basalt. Earth Planet. Sci. Lett. 281, 298–306.
Söderlund, U., Patchett, P.J., Vervoort, J.D., Isachsen, C.E., 2004. The ^{176}Lu decay constant determined by Lu–Hf and U–Pb isotope systematics of Precambrian mafic intrusions. Earth Planet. Sci. Lett. 219, 311–324.
Streck, M.J., Leeman, W.P., Chesley, J., 2007. High–magnesian andesite from Mount Shasta: a product of magma mixing and contamination, not a primitive mantle melt. Geology 35, 351–354.
Sun, S.S., McDonough, W.F., 1989. Chemical and isotopic systematics of oceanic basalts: implications for mantle composition and processes. Geol. Soc. Lond. Spec. Publ. 42, 313–345.
Wang, Q., Wyman, D.A., Xu, J.F., Jian, P., Zhao, Z.H., Li, C.F., Xu, W., Ma, J.L., He, B., 2007. Early cretaceous adakitic granites in the Northern Dabie complex, Central China: Implications for partial melting and delamination of thickened lower crust. Geochim. Cosmochim. Acta 71, 2609–2636.
Wang, J.L., Zhang, Z.M., Xin, D., Feng, L., Fei, Y.U., Wei, W., 2009. Discovery of late cretaceous garnet two–pyroxene granulite in the southern Lhasa terrane, Tibet and its tectonic significances. Acta Petrol. Sin. 25, 1695–1706 (in Chinese with English abstract).
Wen, D.R., Chung, S.L., Song, B., Iizuka, Y., Yang, H.J., Ji, J.Q., Liu, D.Y., Gallet, S., 2008a. Late cretaceous Gangdese intrusions of adakitic geochemical characteristics, SE Tibet: Petrogenesis and tectonic implications. Lithos 105, 1–11.
Wen, D.R., Liu, D.Y., Chung, S.L., Chu, M.F., Ji, J.Q., Zhang, Q., Song, B., Lee, T.Y., Yeh, M.W., Lo, C.H., 2008b. Zircon SHRIMPU–Pb ages of the Gangdese Batholith and implications for Neotethyan subduction in southern Tibet. Chem. Geol. 252, 191–201.
Wu, F.Y., Yang, Y.H., Xie, L.W., Yang, J.H., Xu, P., 2006. Hf isotopic compositions of the standard zircons and baddeleyites used in U–Pb geochronology. Chem. Geol. 234, 105–126.
Xu, J.F., Shinjo, R., Defant, M.J., Wang, Q., Rapp, R.P., 2002. Origin of Mesozoic adakitic intrusive rocks in the Ningzhen area of East China: Partial melting of delaminated lower continental crust? Geology 30, 1111–1114.

Xu, W.C., Zhang, H.F., Luo, B.J., Guo, L., Yang, H., 2015. Adakite–like geochemical signature produced by amphibole–dominated fractionation of arc magmas: an example from the late cretaceous magmatism in Gangdese belt, South Tibet. Lithos 232, 197–210.
Yang, J.H., Wu, F.Y., Chung, S.L., Wilde, S.A., Chu, M.F., 2004. Multiple sources for the origin of granites: Geochemical and Nd/Sr isotopic evidence from the Gudaoling granite and its mafic enclaves, Northeast China. Geochim. Cosmochim. Acta 68, 4469–4483.
Yasukawa, K., Liu, H.J., Fujinaga, K., Machida, S., Haraguchi, S., Ishii, T., Nakamura, K., Kato, Y., 2014. Geochemistry and mineralogy of REY-rich mud in the eastern Indian Ocean. J. Asian Earth Sci. 93, 25–36.
Yaxley, G.M., Green, D.H., 1998. Reactions between eclogite and peridotite: mantle refertilisation by subduction of oceanic crust. Schweiz. Mineral. Petrogr. Mitt. 78, 243–255.
Yin, A., Harrison, T.M., 2000. Geologic Evolution of the Himalayan–Tibetan Orogen. Annu. Rev. Earth Planet. Sci. 28, 211–280.
Zhang, S.Q., Mahoney, J.J., Mo, X.X., Ghazi, A.M., Milani, L., Crawford, A.J., Guo, T.Y., Zhao, Z.D., 2005. Evidence for a Widespread Tethyan Upper Mantle with Indian–Ocean–Type Isotopic Characteristics. J. Petrol. 46, 829–858.
Zhang, Z.M., Zhao, G.C., Santosh, M., Wang, J.L., Dong, X., Shen, K., 2010. Late cretaceous charnockite with adakitic affinities from the Gangdese batholith, southeastern Tibet: evidence for Neo–Tethyanmid–ocean ridge subduction? Gondwana Res. 17, 615–631.
Zhao, Z.D., Mo, X.X., Dilek, Y., Niu, Y.L., Depaolo, D.J., Robinson, P., Zhu, D.C., Sun, C.G., Dong, G.C., Zhou, S., Luo, Z.H., Hou, Z.Q., 2009. Geochemical and Sr–Nd–Pb–O isotopic compositions of the post–collisional ultrapotassic magmatism in SW Tibet: Petrogenesis and implications for Indiaintra–continental subduction beneath southern Tibet. Lithos 113, 190–212.
Zheng, Y.C., Hou, Z.Q., Li, Q.Y., Sun, Q.Z., Liang, W., Fu, Q., Li, W., Huang, K.X., 2012a. Origin of late Oligocene adakitic intrusives in the southeastern Lhasa terrane: evidence from in situ zircon U–Pb dating, Hf–O isotopes, and whole–rock geochemistry. Lithos 148, 296–311.
Zheng, Y.C., Hou, Z.Q., Li, W., Liang, W., Huang, K.X., Li, Q.Y., Sun, Q.Z., Fu, Q., Zhang, S., 2012b. Petrogenesis and geological implications of the Oligocene Chongmuda–Mingzeadakite–like intrusions and their mafic enclaves, southern Tibet. The Journal of Geology 120, 647–669.
Zheng, Y.C., Hou, Z.Q., Gong, Y.L., Liang, W., Sun, Q.Z., Zhang, S., Fu, Q., Huang, K.X., Li, Q.Y., Li, W., 2014. Petrogenesis of cretaceous adakite–like intrusions of the Gangdese Plutonic Belt, southern Tibet: Implications for mid–ocean ridge subduction and crustal growth. Lithos 190, 240–263.
Zheng, Y.C., Hou, Z.Q., Fu, Q., Zhu, D.C., Liang, W., Xu, P.Y., 2016. Mantle inputs to Himalayan anatexis: Insights from petrogenesis of the Miocene Langkazi leucogranite and its dioritic enclaves. Lithos 264, 125–140.
Zhu, D.C., Pan, G.T., Chung, S.L., Liao, Z.L., Wang, L.Q., Li, G.M., 2008. SHRIMP Zircon Age and Geochemical Constraints on the Origin of lower Jurassic Volcanic Rocks from the Yeba Formation, Southern Gangdese, South Tibet. Int. Geol. Rev. 50, 442–471.
Zhu, D.C., Mo, X.X., Niu, Y.L., Zhao, Z.D., Wang, L.Q., Liu, Y.S., Wu, F.Y., 2009a. Geochemical investigation of early cretaceous igneous rocks along an east–west traverse throughout the Central Lhasa Terrane, Tibet. Chem. Geol. 268, 298–312.
Zhu, D.C., Zhao, Z.D., Pan, G.T., Lee, H.Y., Kang, Z.Q., Liao, Z.L., Wang, L.Q., Li, G.M., Dong, G.C., Liu, B., 2009b. Early cretaceous subduction–relatedadakite–like rocks of the Gangdese Belt, southern Tibet: Products of slab melting and subsequent melt–peridotite interaction? J. Asian Earth Sci. 34, 298–309.
Zhu, D.C., Zhao, Z.D., Niu, Y.L., Mo, X.X., Chung, S.L., Hou, Z.Q., Wang, L.Q., Wu, F.Y., 2011. The Lhasa Terrane: Record of a microcontinent and its histories of drift and growth. Earth Planet. Sci. Lett. 301, 241–255.
Zhu, D.C., Wang, Q., Zhao, Z.D., Chung, S.L., Cawood, P.A., Niu, Y.L., Liu, S.A., Wu, F.Y., Mo, X.X., 2015. Magmatic record of India-Asia collision. Sci. Rep. 5, 14289.
Zhu, D.C., Wang, Q., Cawood, P.A., Zhao, Z.D., Mo, X.X., 2017. Raising the Gangdese Mountains in southern Tibet: Raising the Gangdese Mountains. J. Geophys. Res. Solid Earth 122, 214–223.